IASPEI Book (0000) **000**, 000–000

Spectral-Element Analysis in Seismology

Emmanuel Chaljub[1], Dimitri Komatitsch[2,4], Jean-Pierre Vilotte[3],
Yann Capdeville[3], Bernard Valette[5] and Gaetano Festa[3]

[1] *Laboratoire de Géophysique Interne et de Tectonophysique, BP 53, 38041 Grenoble Cedex 9, France*
[2] *Seismological Laboratory, California Institute of Technology, 1200 East California Boulevard, Pasadena, California 91125, USA*
[3] *Institut de Physique du Globe, 4 place Jussieu, 75252 Paris Cedex 05, France*
[4] *now at: Laboratoire de Modélisation et d'Imagerie en Géosciences CNRS FRE 2639, Université de Pau et des Pays de l'Adour, BP 1155, 64013 Pau Cedex, France*
[5] *Laboratoire de Géophysique Interne et de Tectonophysique, Université de Savoie, 73376 Le Bourget-du-Lac Cedex, France.*

SUMMARY
We present a review of the application of the spectral-element method to regional and global seismology. This technique is a high-order variational method that allows one to compute accurate synthetic seismograms in three-dimensional heterogeneous Earth models with deformed geometry. We first recall the strong and weak forms of the seismic wave equation with a particular emphasis set on fluid regions. We then discuss in detail how the conditions that hold on the boundaries, including coupling boundaries, are honored. We briefly outline the spectral-element discretization procedure and present the time-marching algorithm that makes use of the diagonal structure of the mass matrix. We show examples that illustrate the capabilities of the method and its interest in the context of the computation of three-dimensional synthetic seismograms.

Key words: DtN operator – elastodynamics – global seismology – regional seismology – numerical modeling – Perfectly Matched Layers – potential formulation – self-gravitation – spectral-element method – surface waves – synthetic seismograms – topography.

1 INTRODUCTION

Coming along with the tremendous increase of computational power, the development of numerical methods for the accurate calculation of synthetic seismograms in three-dimensional (3D) models of the Earth has been the subject of a continuous effort in the past thirty years.

Among the different numerical approaches used to model the propagation of seismic waves, the most popular is probably the finite-difference (FD) method, in which partial derivatives are approximated by discrete operators involving differences between adjacent grid points. The literature about FD methods is huge, from the historical articles of Alterman & Karal (1968), Alford et al. (1974), Kelly et al. (1976), Madariaga (1976) and Virieux (1986) to realistic applications to 3D strong ground motion (e.g., Frankel & Vidale 1992; Frankel 1993; Olsen & Archuleta 1996; Pitarka et al. 1998; Olsen 2000). However, in spite of recent improvements such as optimal or compact operators (e.g., Zingg et al. 1996; Zingg 2000), FD methods still suffer from severe limitations regarding (i) the calculation of accurate surface waves; (ii) the ability to account for deformed geometries, in particular to deal with topography at the free surface; and (iii) the possibility to adapt the size of the grid to the seismic wavelengths under consideration in order to save computing time and memory. As an illustration of such limitations, it is worth noting that FD methods have not been able to tackle the challenge posed by global seismology, except in simplified geometries (e.g., Igel & Weber 1995, 1996; Chaljub & Tarantola 1997).

Boundary-element methods based upon integral representation theorems combined with discrete wavenumber expansions of Green's functions have been proposed to incorporate realistic surface and interface topography (see e.g., Bouchon

(1996) and references therein, Bouchon & Sánchez-Sesma (2006) (this book), Chen (2006) (this book)). However, these methods are restricted to media consisting of a finite number of homogeneous layers, and lead to large ill-conditioned linear matrix systems in 3D applications.

Spectral and pseudo-spectral methods have also been applied to regional (e.g., Tessmer & Kosloff 1994; Carcione 1994) and (axisymmetric) global (e.g., Furumura et al. 1998, 1999) elastodynamics, outperforming FD methods regarding the very small amount of numerical dispersion obtained with only a small number of grid points per wavelength that can be chosen very close to the theoretical Nyquist sampling limit. However, because of the global nature of the polynomial basis chosen, these methods are restricted to smooth geological media and cannot be applied to complicated geometries or sharp heterogeneities. Like FD methods, they are also unable to model surface waves with the same accuracy as body waves because of the one-way treatment that needs to be performed in order to implement the free-surface condition (e.g., Carcione 1994).

Although well suited to handle complex geometries and interface conditions, classical finite-element methods (FEM) have not very often been applied to elastodynamics (e.g., Lysmer & Drake 1972; Toshinawa & Ohmachi 1992; Bao et al. 1998) because of the large amount of numerical dispersion related to the low-order polynomial bases used (Marfurt 1984), and also because of the computational effort needed to solve the resulting large linear systems on parallel computers with distributed memory.

The scope of this article is to review recent progress in the application of the spectral-element method (SEM) to regional and global seismology. The SEM was introduced twenty years ago in computational fluid mechanics by Patera (1984) and Maday & Patera (1989). It is a high-order variational method that retains the ability of FEMs to handle complicated geometries while keeping the exponential convergence rate of spectral methods. This last property explains the term ‘spectral element’ that was chosen by Patera (1984), which can be confusing because the method works in the time domain, not in the frequency domain. Applications of the SEM to two-dimensional (2D) (e.g., Cohen et al. 1993; Priolo et al. 1994) and 3D elastodynamics (e.g., Komatitsch 1997; Faccioli et al. 1997; Komatitsch & Vilotte 1998; Seriani 1998; Komatitsch & Tromp 1999; Komatitsch et al. 2004; Liu et al. 2004) have shown that very high accuracy and low numerical dispersion are obtained and that an efficient parallel implementation is possible. The SEM has further been applied successfully to global seismology in fully 3D Earth models (Chaljub 2000; Komatitsch & Tromp 2002a,b; Komatitsch et al. 2002; Chaljub et al. 2003; Komatitsch et al. 2003; Chaljub & Valette 2004) by taking advantage of its great geometrical flexibility. It is also worth mentioning other geophysical applications of the method to spherical geometry, such as the resolution of the shallow water equation (Taylor et al. 1997).

In this article we first recall the wave equation, with particular emphasis on the potential formulation that is used in the fluid parts of the model. We present the method used to couple the SEM with other methods for static or dynamic problems, and to design adapted interface operators for specific problems such as the computation of the exterior gravity potential and the coupling with a modal solution in the frequency domain. We further recall the weak form of the equations and detail how boundary conditions are honored, in particular at fluid-solid interfaces. We then briefly outline the spectral-element discretization and review technical aspects relevant to mesh generation and to the choice of parameters for accurate calculations. Details are also given on how to adapt the time-marching algorithm in order to include Perfectly Matched Layers, attenuation, rotation and self-gravitation. Examples of application to regional and global seismology are finally presented, which illustrate the potentiality of the method in the context of 3D geophysical problems.

2 THE WAVE EQUATION IN REGIONAL AND GLOBAL SEISMOLOGY

In this section we recall the seismic wave equation in the general framework of a self-gravitating, rotating Earth as well as the simpler formulation relevant at a regional scale. We provide a potential decomposition of the displacement field in the fluid regions. We also recall the continuity conditions that hold on the internal interfaces and we define a set of boundaries through which the spectral-element solution can be coupled to solutions obtained based upon other methods. Finally, we derive the weak form of the equations in the fluid and solid regions. The reader is referred to e.g. Aki & Richards (1980) for a complete treatment of seismic wave propagation problems and to e.g. Dahlen & Tromp (1998) for a general discussion of global seismology.

2.1 General framework

Let us start with a description of the geometry of the problem and define some notations. Let V denote the spatial domain in which we are interested in modeling seismic wave propagation. V consists either of the whole Earth or of a portion of it, as depicted in Figure 1. The solid and fluid regions of V are denoted by V_S and V_F, respectively, and

Σ_{SS} (resp. Σ_{FS}) stands for the set of solid-solid (resp. fluid-solid) interfaces. We consider the ocean-crust boundary as a particular interface, which we denote by Σ_{OC}.

Finally, two interfaces are introduced depending on the size of the problem: the outer spherical boundary $\partial_{\mathcal{B}}$ that will be used when accounting for self-gravitation at the global scale, and the absorbing boundary Σ_{abs} that will be needed in regional applications.

2.2 Reference configuration

A seismic wave is assumed to be a small perturbation about a rotating reference configuration in which the elastic medium is stressed due to self-gravitation. The effect of deviatoric pre-stress on wave propagation being small (e.g., Valette 1986), the initial stress is usually assumed to be hydrostatic. Under this assumption, the static equilibrium in the reference configuration is

$$\nabla \cdot \mathbf{T}^0 \;=\; -\nabla p^0 \;=\; \rho \nabla \phi \;, \tag{1}$$

where $\mathbf{T}^0$ is the initial Cauchy stress tensor, p^0 is the initial hydrostatic pressure, ρ is density and ϕ is the geopotential, which is related to the non-rotating gravity potential ϕ' by

$$\phi(\mathbf{r}) \;=\; \phi'(\mathbf{r}) - \frac{1}{2}\left(\Omega^2 r^2 - (\boldsymbol{\Omega}\cdot\mathbf{r})^2\right) \;, \tag{2}$$

where $\mathbf{r}$ denotes position and $\boldsymbol{\Omega}$ is the Earth's angular velocity vector. Gravity is defined from the geopotential by $\mathbf{g} = -\nabla\phi$, and the non-rotating gravity potential is obtained by solving Poisson's equation:

$$\nabla^2 \phi' = \begin{cases} 4\pi G \rho & \text{in } V \;, \\ 0 & \text{outside } V \;, \end{cases} \tag{3}$$

together with the additional requirements that both ϕ' and $\nabla\phi' \cdot \hat{\mathbf{n}}$ be continuous and that the regularity condition

$$\lim_{\|\mathbf{r}\|\to\infty} \phi'(\mathbf{r}) = 0 \;, \tag{4}$$

hold.

The equilibrium equation (1) implies that the level surfaces of density, geopotential and pressure coincide, which imposes strong constraints on admissible distributions of density within the medium. In what follows, we use the so-called quasi-hydrostatic approximation, in which lateral variations of density are allowed but where the effects of deviatoric pre-stress are ignored (see Dahlen & Tromp 1998, p. 101).

2.3 The gravito-elastodynamic equations

The wave equation is obtained through a first-order Lagrangian perturbation of the equilibrium equation (1). We write it under the general form:

$$\ddot{\mathbf{u}} \;+\; 2\,\boldsymbol{\Omega}\times\dot{\mathbf{u}} \;+\boldsymbol{\mathcal{A}}(\dot{\mathbf{u}},\mathbf{u}) \;=\; \frac{1}{\rho}\,\mathbf{f} \;, \tag{5}$$

where a dot over a symbol indicates time differentiation. In Eq. (5), $\mathbf{u}$ is the Lagrangian perturbation of displacement and $\boldsymbol{\mathcal{A}}$ denotes the elastic-gravitational operator. The dependence of $\boldsymbol{\mathcal{A}}$ on velocity accounts for possible attenuation, the treatment of which is postponed to Appendix A1.

In the case of global seismology, the seismic source $\mathbf{f}$ is usually represented by a point moment tensor:

$$\mathbf{f}(\mathbf{r},t) \;=\; -\nabla\cdot\left(\mathbf{m}_0\,\delta(\mathbf{r}-\mathbf{r}_s)\right)\,g(t) \;, \tag{6}$$

where $\mathbf{r}_s$ is the position of the source, $\mathbf{m}_0$ is a given seismic moment tensor, and $g(t)$ is the source time function. The spatial extent and the kinematics of the source can be accounted for by considering a superimposition of punctual sources with different onset time, moment tensor and time history (e.g., Tsuboi et al. 2003).

The most general form of the elastic-gravitational operator is

$$\rho\,\boldsymbol{\mathcal{A}}(\mathbf{u}) \;=\; -\nabla\cdot\mathbf{T}(\mathbf{u}) \;-\; \nabla\left(\rho\mathbf{u}\cdot\mathbf{g}\right) \;+\; \{\nabla\cdot(\rho\mathbf{u})\}\;\mathbf{g} \;+\; \rho\nabla\psi(\mathbf{u}) \;, \tag{7}$$

where $\mathbf{T}$ is the Lagrangian incremental stress tensor and $\psi(\mathbf{u})$ is the Eulerian perturbation of the gravitational potential ϕ', also referred to as the mass redistribution potential. The first term on the right-hand side of Eq. (7) represents the internal elastic forces, while the second term accounts for hydrostatic pre-stress. The remaining terms reflect the perturbation of gravity, which is twofold: a local term in which only density is perturbed and a global term that accounts for the perturbation of the gravitational field.

The Lagrangian incremental stress tensor is related to the infinitesimal strain tensor $\boldsymbol{\varepsilon}(\mathbf{u}) = \frac{1}{2}\left(\nabla\mathbf{u} + \nabla^T\mathbf{u}\right)$ by Hooke's law:

$$\mathbf{T}_{ij}(\mathbf{u}) \;=\; d_{ijkl}\,\varepsilon_{kl}(\mathbf{u}) \;, \tag{8}$$

in which the fourth-order tensor d is obtained from the classical elastic tensor c (i.e., that relating the Eulerian Cauchy stress tensor to the infinitesimal strain tensor) by

$$d_{ijkl} \;=\; c_{ijkl} - \mathbf{T}^0_{ij}\delta_{kl} + \mathbf{T}^0_{ik}\delta_{jl} + \mathbf{T}^0_{jk}\delta_{il}, \tag{9}$$

where δ is the Kronecker delta.

Whenever intrinsic attenuation is included, or when Perfectly Matched Layers are used in order to absorb energy in the context of regional applications, the stress-strain relation (8) has to be modified. The reader is referred to Appendix A for details on how to derive the modified Hooke's law that needs to be used in such a case.

Finally, the mass redistribution potential is obtained by solving a Poisson-Laplace equation over the entire space:

$$\nabla^2\psi(\mathbf{u}) = \begin{cases} -4\pi G\,\nabla\cdot(\rho\mathbf{u}) & \text{in } V \ , \\ 0 & \text{outside } V \ . \end{cases} \tag{10}$$

2.3.1 *Cowling approximation*

Ignoring the perturbation of the gravitational potential in Eq. (7) yields the so-called Cowling approximation (Cowling 1941), in which:

$$\rho\,\boldsymbol{\mathcal{A}}(\mathbf{u}) \;=\; -\nabla\cdot\mathbf{T}(\mathbf{u}) \;-\; \nabla\left(\rho\mathbf{u}\cdot\mathbf{g}\right) \;+\; \{\nabla\cdot(\rho\mathbf{u})\}\;\mathbf{g}\ . \tag{11}$$

The latter form has been used by Chaljub (2000); Komatitsch & Tromp (2002b); Capdeville et al. (2003a,b) and Chaljub et al. (2003) because in that context it is not necessary to solve the unbounded Poisson-Laplace equation (10).

Note that even in the Cowling approximation, one needs to solve Eq. (3) in the entire space for the 3D gravitational potential. This step was neglected by Komatitsch & Tromp (2002b) and Capdeville et al. (2003b), who used the alternative approximation:

$$\rho\,\boldsymbol{\mathcal{A}}(\mathbf{u}) \;=\; -\nabla\cdot\mathbf{T}(\mathbf{u}) \;-\; \nabla\left(\rho\mathbf{u}\cdot\mathbf{g}'\right) \;+\; \{\nabla\cdot(\rho\mathbf{u})\}\;\mathbf{g}'\ , \tag{12}$$

where $\rho = \rho'+\delta\rho$ consists of lateral variations $\delta\rho$ superimposed to a one-dimensional (1D) spherically-symmetric profile ρ', and where $\mathbf{g}'$ is the (analytical) gravity vector computed from ρ'.

A consistent implementation of the Cowling approximation, i.e., that includes lateral variations in gravity, is proposed in Appendix B2 based upon the work of Chaljub & Valette (2004).

2.3.2 *Regional seismology*

Self-gravitation and rotation can be safely neglected at the periods considered in regional applications (see e.g., Dahlen & Tromp 1998, p. 142). The wave equation can then be written directly in Eulerian form using Eq. (1), without the Coriolis term on the left-hand side and with

$$\rho\,\boldsymbol{\mathcal{A}}(\mathbf{u}) \;=\; -\nabla\cdot\mathbf{T}(\mathbf{u})\ . \tag{13}$$

In Eq. (13), $\mathbf{T}$ is the Cauchy stress tensor, which satisfies Hooke's law (8) in which d is replaced with the usual elastic tensor c by virtue of (9).

2.4 Potential formulation in fluid regions

Accounting for the propagation of seismic waves in media with both fluid and solid regions is known to be a difficult task in the finite-element method: one cannot simply set the shear modulus to zero in the fluid because spurious (shear) oscillations appear and evolve without any numerical control (e.g., Hamdi et al. 1978) due to the fact the wave equation, when formulated in displacement, has too many degrees of freedom in the fluid. One must therefore impose an additional constraint to prevent spurious modes from developing. From a numerical point of view, the critical aspect is to correctly discretize the null space $\mathcal{N}(\mathcal{A})$ of the elastic-gravitational operator (Bermúdez & Rodríguez 1994). An alternative to the discretization of $\mathcal{N}(\mathcal{A})$ is to resort to a potential formulation in order to eliminate the shear part of displacement.

In what follows, we recall the wave equation in the fluid and present a general approach to derive the potential formulation to be used in global or regional seismology, which generalizes those of Komatitsch et al. (2000); Komatitsch & Tromp (2002b); Chaljub et al. (2003) and Chaljub & Valette (2004) to the case of a self-gravitating, rotating, arbitrarily-stratified fluid.

2.4.1 Fluid regions

In the fluid regions, the stress tensor $\mathbf{T}(\mathbf{u})$ takes the form:

$$\mathbf{T}(\mathbf{u}) \;=\; -\delta p\, \mathbf{I} \;=\; \rho c^2\, \nabla\cdot\mathbf{u}\, \mathbf{I}\;, \tag{14}$$

where δp is the Lagrangian pressure perturbation, c is the P-wave velocity and $\mathbf{I}$ denotes the second-order identity tensor. The gravito-elastic operator can be rewritten in the general form

$$-\boldsymbol{\mathcal{A}}(\mathbf{u}) \;=\; \nabla\left[c^2\nabla\cdot\mathbf{u} \;+\; \mathbf{u}\cdot\mathbf{g} \;-\; \psi(\mathbf{u})\right] \;+\; c^2\,\nabla\cdot\mathbf{u}\,\mathbf{s}\;, \tag{15}$$

where $\mathbf{s}$ is defined by

$$\mathbf{s} \;=\; \frac{\nabla\rho}{\rho} \;-\; \frac{\mathbf{g}}{c^2}\;, \tag{16}$$

and is related to the so-called Brunt-Väisälä squared frequency N^2 by

$$N^2 \;=\; \mathbf{s}\cdot\mathbf{g} \;=\; \frac{1}{\rho}\left(\nabla\rho \;-\; \frac{\rho}{c^2}\,\mathbf{g}\right)\cdot\mathbf{g}\;. \tag{17}$$

A fluid is said to be stably stratified if N^2 is positive. In this case, the motion of a small fluid region moved away from its equilibrium position is oscillatory, with a characteristic frequency equal to N. The restoring force in this process being buoyancy, N is often referred to as the buoyancy frequency. The corresponding oscillations are referred to as internal gravity waves in the ocean or in the atmosphere and as the core undertones in the Earth's outer core. Wherever $N^2 < 0$, the stratification is said to be unstable because the motion of a small fluid region can diverge locally. This situation corresponds to the onset of convection. Finally, a fluid that has $N^2 = 0$ is said to be neutrally stratified. Note that the spectrum of the elastic-gravitational operator acquires a continuous non-seismic low-frequency part when $N^2 \neq 0$ (Valette 1989), which makes a numerical solution difficult to design. In what follows, we do not make any assumption about the stratification within the fluid, but let us mention that we do not intent to compute the non-seismic part of the spectrum.

Upon substituting Eq. (15) into Eq. (1), we obtain the wave equation in the fluid regions:

$$\ddot{\mathbf{u}} \;=\; \nabla\left[c^2\nabla\cdot\mathbf{u} \;+\; \mathbf{u}\cdot\mathbf{g} \;-\; \psi(\mathbf{u})\right] \;+\; c^2\,\nabla\cdot\mathbf{u}\,\mathbf{s} -\; 2\,\boldsymbol{\Omega}\times\dot{\mathbf{u}}\;. \tag{18}$$

2.4.2 Potential formulation

Considering the wave equation (18), we assume that the displacement field in the fluid takes the form:

$$\mathbf{u} \;=\; \nabla\chi \;+\; \zeta\mathbf{s} \;+\; \mathbf{w}\;, \tag{19}$$

where χ and ζ denote two arbitrary potentials and $\mathbf{w}$ is an arbitrary vector field. Differentiating twice with respect to time and identifying each term with the right-hand side of Eq. (18), we obtain a system of two scalar and one vector wave equations:

$$\ddot{\zeta} = c^2\,\nabla\cdot(\nabla\chi + \zeta\,\mathbf{s} + \mathbf{w})\;, \tag{20}$$

$$\ddot{\chi} = \ddot{\zeta} \;+\; (\nabla\chi + \mathbf{w})\,\cdot\mathbf{g} \;+\; N^2\,\zeta \;-\; \psi(\mathbf{u})\;, \tag{21}$$

$$\ddot{\mathbf{w}} = -\,2\,\boldsymbol{\Omega}\times\left(\nabla\dot{\chi} + \dot{\zeta}\,\mathbf{s} - 2\,\boldsymbol{\Omega}\times\dot{\mathbf{w}}\right)\;. \tag{22}$$

Note that the displacement field defined by Eq. (19) with χ, ζ and $\mathbf{w}$ satisfying Eqs. (20–22) is the unique solution to the wave equation (18), even though the choice of the potential decomposition is arbitrary. With the choice made in Eq. (19), the two potentials ζ and χ are respectively related to the Lagrangian and Eulerian perturbations of pressure through

$$\delta p = -\rho\,\ddot{\zeta} \tag{23}$$

and

$$p' = \delta p - \rho\,\mathbf{u}\cdot\mathbf{g} = -\rho\,(\ddot{\chi} + \psi(\mathbf{u}))\;. \tag{24}$$

Note that for a neutrally stratified fluid ($\mathbf{s} = \mathbf{0}$), only one scalar potential is required. Eqs. (20) and (21) can indeed be combined into

$$\ddot{\chi} = c^2\,\nabla\cdot(\nabla\chi + \mathbf{w}) \;+\; (\nabla\chi + \mathbf{w})\,\cdot\mathbf{g} \;-\; \psi(\mathbf{u})\;. \tag{25}$$

Setting $\mathbf{w} = \mathbf{0}$ and $\psi(\mathbf{u}) = 0$ in (25), and noting that $\mathbf{g} = (c^2/\rho)\,\nabla\rho$ for a neutrally stratified fluid, one obtains the same equation as in Komatitsch & Tromp (2002b) and Chaljub et al. (2003) for the velocity potential. For the sake of generality, we introduce a second potential such that $\ddot{\zeta} = \ddot{\chi} - (\nabla\chi + \mathbf{w})\,\cdot\mathbf{g} + \psi(\mathbf{u})$, so that Eq. (23) defining the Lagrangian perturbation of pressure still holds.

Finally, note that the expression of displacement (19) also has to be used in Eq. (10) when solving for the mass redistribution potential in the fluid regions V_F.

2.4.3 Regional seismology

When self-gravitation is neglected, it is not convenient to deal with the general expression (15). Instead, we consider the elastic operator obtained by inserting (14) into (13):

$$-\rho\boldsymbol{\mathcal{A}}(\mathbf{u}) \;=\; \nabla\left[\rho c^2 \nabla\cdot\mathbf{u}\right] \;. \tag{26}$$

The process used to derive the potential formulation is the same as above: we write the wave equation

$$\ddot{\mathbf{u}} \;=\; \frac{1}{\rho}\nabla\left[\rho c^2 \nabla\cdot\mathbf{u}\right] \;, \tag{27}$$

from which we assume that the displacement field should have the form

$$\mathbf{u} \;=\; \frac{1}{\rho}\nabla\left(\rho\,\zeta\right) \;, \tag{28}$$

where ζ is a scalar potential. The equation governing the evolution of ζ is obtained by differentiating Eq. (28) twice with respect to time and identifying it with the right-hand side of Eq. (27):

$$\ddot{\zeta} \;=\; c^2\nabla\cdot\left(\frac{1}{\rho}\nabla\left(\rho\,\zeta\right)\right) \;. \tag{29}$$

Note that we have chosen the potential in Eq. (28) so that pressure is $p = -\rho\,\ddot{\zeta}$, as in the self-gravitating case, and therefore our potential differs from that used by Komatitsch & Tromp (1999). As mentioned previously, this is not a problem because the decomposition is not unique, only the solution to the wave equation is.

2.5 Initial and boundary conditions

In order to define a unique solution to the wave equation (5) and (10), we must provide both initial and boundary conditions.

2.5.1 Initial conditions

According to the assumption that the medium is initially at rest, the initial conditions require that displacement and velocity vanish in the reference configuration. We thus set $\mathbf{u} = \dot{\mathbf{u}} = \mathbf{0}$ in the solid and $\chi = \dot{\chi} = \zeta = \dot{\zeta} = 0$ and $\mathbf{w} = \dot{\mathbf{w}} = \mathbf{0}$ in the fluid at $t = 0$. There is no perturbation of the gravitational potential in the initial configuration, therefore $\psi(\mathbf{u})$ is also set to zero.

Taking the initial conditions into account, the precession equation (22) governing the evolution of $\mathbf{w}$ can be integrated in time in order to get a form closer to that given by Komatitsch & Tromp (2002b):

$$\dot{\mathbf{w}} + 2\,\boldsymbol{\Omega}\times\mathbf{w} \;=\; -\;2\,\boldsymbol{\Omega}\times\left(\nabla\chi + \zeta\,\mathbf{s}\right) \;. \tag{30}$$

2.5.2 Internal boundary conditions

First, for the solid regions to remain in welded contact, the displacement must be continuous across the solid-solid interfaces that are present at the contact between layers in the geological medium. This can be written as

$$[\mathbf{u}]_{\Sigma_{SS}} \;=\; \mathbf{0} \;, \tag{31}$$

where $[\;\;]_{\Sigma_{SS}}$ stands for the jump operator across Σ_{SS}, defined in accordance with the unit normal vector $\hat{\mathbf{n}}$: $[\mathbf{u}]_{\Sigma_{SS}} = \mathbf{u}^+ - \mathbf{u}^-$, with $\hat{\mathbf{n}}$ pointing from the $-$ to the $+$ side.

Then, because we assume that we deal with inviscid fluids only, any tangential slip is allowed at the fluid-solid interfaces and therefore the kinematic condition to be used is the continuity of normal displacement:

$$[\mathbf{u}\cdot\hat{\mathbf{n}}]_{\Sigma_{FS}} \;=\; 0 \;, \tag{32}$$

which, using the decomposition (19), gives

$$\mathbf{u}\cdot\hat{\mathbf{n}} \;=\; \left(\nabla\chi \;+\; \zeta\,\mathbf{s} \;+\; \mathbf{w}\right)\cdot\hat{\mathbf{n}} \quad \text{on } \Sigma_{FS} \;. \tag{33}$$

Traction is continuous across every interface of the medium in virtue of the action-reaction principle. Let Σ stand for a particular internal boundary, we have

$$[\mathbf{T}(\mathbf{u})\cdot\hat{\mathbf{n}}]_{\Sigma} \;=\; \mathbf{0} \;. \tag{34}$$

According to (23), this can be rewritten on the fluid-solid interfaces Σ_{FS} as

$$\mathbf{T}(\mathbf{u}) \cdot \hat{\mathbf{n}} \;=\; \rho \ddot{\zeta}\, \hat{\mathbf{n}} \; . \tag{35}$$

Finally, the mass redistribution potential is continuous across every interface Σ:

$$[\psi(\mathbf{u})]_\Sigma \;=\; 0 \; , \tag{36}$$

but its normal derivative can be discontinuous if a density contrast is present:

$$[\nabla \psi(\mathbf{u}) \cdot \hat{\mathbf{n}}]_\Sigma \;=\; -4\pi G \; [\rho]_\Sigma \, \mathbf{u} \cdot \hat{\mathbf{n}} \; . \tag{37}$$

2.6 Coupling boundaries

In some situations, we may be interested in solving the wave equation outside the computational domain V based on another method than the SEM. This is typically the case for applications in unbounded domains, for example when computing the perturbation of the gravitational potential at the global scale or when imposing absorbing boundary conditions at the regional scale. This situation also arises when a direct method, either exact or approximate, is available to solve the wave equation outside V. In some applications in global seismology for example, one may assume that the lower mantle and the core are radially stratified and that lateral heterogeneities are only present in the upper mantle. In such a case, it is interesting to use a simpler method to compute the solution in the 1D regions of the model and to restrict the use of the SEM to the mantle and the crust, where 3D heterogeneities are present. Another example arises when accounting for the presence of the oceans in global seismology applications: in many (but not all) seismological studies performed at the global scale, the thickness of the oceans is usually one order of magnitude smaller than the seismic wavelengths of interest, allowing one to use an approximation of the wave equation in the water layer. In all cases, the exterior domain, say W, can be accounted for by means of a boundary condition defined on the interface between V and W. In what follows, we explain how to derive such a condition by introducing a so-called Dirichlet-to-Neumann operator on the coupling boundary. Detailed expressions of the coupling operators needed in practical situations are given in Appendix B.

2.6.1 Coupling principle

Suppose that we know how to solve the wave equation (5) and (10) in a region W, and let Γ stand for the interface between W and the computational domain V. We can assume without loss of generality that Γ is a solid-solid boundary. Then, according to Eqs. (31) and (34), both displacement and traction must match on Γ at all times. This means that $\forall\, t \in [0, T]$:

$$\mathbf{u}_t^V = \mathbf{u}_t^W \; , \tag{38}$$

$$\mathbf{T}(\mathbf{u}_t^V) \cdot \hat{\mathbf{n}} = \mathbf{T}(\mathbf{u}_t^W) \cdot \hat{\mathbf{n}} \; , \tag{39}$$

where the superscript denotes the region where the solution is defined. Let us now recall that for the wave equation to be well-posed in region V or W, it is sufficient to know either traction or displacement on Γ at all times. The principle of the coupling is to mix these conditions: for example to solve in V with the prescribed traction $\mathbf{T}(\mathbf{u}_t^W) \cdot \hat{\mathbf{n}}$ on Γ and to solve in W with the prescribed displacement $\mathbf{u}_t^V$ on Γ. The key issue to apply this strategy is to compute the surface traction from a given displacement on Γ. This process is referred to as a Dirichlet-to-Neumann (DtN) operator, in reference to the nomenclature of classical boundary conditions in elasticity (e.g., Givoli 1992).

Let then $\boldsymbol{\mathcal{D}}_t^W$ denote the DtN operator that computes the surface traction on Γ at time t. The superscript W indicates that the operator is based upon the knowledge of the solution in region W. In order to be properly defined, $\boldsymbol{\mathcal{D}}_t^W$ must be applied to the entire history of surface displacements:

$$\boldsymbol{\mathcal{D}}_t^W(\mathbf{u}_{t' \leq t}^W) = \mathbf{T}(\mathbf{u}_t^W) \cdot \hat{\mathbf{n}} \; . \tag{40}$$

The boundary condition to be used in order to solve the wave equation in V can then be expressed formally as

$$\mathbf{T}(\mathbf{u}_t^V) \cdot \hat{\mathbf{n}} \;=\; \boldsymbol{\mathcal{D}}_t^W(\mathbf{u}_{t' \leq t}^V) \; . \tag{41}$$

The reader is referred to Appendix B for detailed expressions of DtN operators needed in practical applications to (i) couple the SEM with a normal-mode solution in the frequency domain (see Appendix B1), (ii) take into account gravity perturbations induced by low-frequency seismic waves (see Appendix B2) or (iii) approximate the elastic response of the ocean in global seismology applications (see Appendix B3).

2.7 Weak formulation

The SEM is a particular case of the finite-element method and is therefore based on the variational, or weak, form of the wave equation. Let us recall the formulation in the solid and fluid regions with a particular emphasis on how to honor the boundary conditions.

2.7.1 Solid regions

To obtain the weak form of the wave equation in the solid we first take the $L^2(V_S)$ scalar product of Eq. (5) with an admissible displacement field $\tilde{\mathbf{u}}$:

$$\int_{V_S} \rho\,(\ddot{\mathbf{u}} + 2\,\boldsymbol{\Omega}\times\dot{\mathbf{u}})\cdot\tilde{\mathbf{u}}\;dV \;+\; \int_{V_S} \rho\,\boldsymbol{\mathcal{A}}(\mathbf{u})\cdot\tilde{\mathbf{u}}\;dV \;=\; \int_{V_S} \mathbf{f}\cdot\tilde{\mathbf{u}}\;dV\;. \tag{42}$$

Then, in the last term of the left-hand side we integrate by parts the divergence of the stress tensor to remove the second-order spatial derivatives of the displacement. We obtain

$$-\int_{V_S} \nabla\cdot\mathbf{T}(\mathbf{u})\cdot\tilde{\mathbf{u}}\;dV \;=\; \int_{V_S} \mathbf{T}(\mathbf{u})\,\cdot\,\nabla\tilde{\mathbf{u}}\;dV \;-\; \int_{\Sigma} \mathbf{T}(\mathbf{u})\cdot\hat{\mathbf{n}}\,\cdot\,\tilde{\mathbf{u}}\;dS\;, \tag{43}$$

where Σ comprises the free surface ∂_V, the fluid-solid interfaces Σ_{FS}, the ocean-crust boundary Σ_{OC}, the coupling boundaries Γ, and the absorbing boundaries Σ_{abs}. We then impose the free surface condition by setting the traction to zero on $\partial_V \cap \partial_{V_S}$, which gives:

$$\int_{\Sigma} \mathbf{T}(\mathbf{u})\cdot\hat{\mathbf{n}}\,\cdot\,\tilde{\mathbf{u}}\;dS \;=\; \int_{\Sigma_{FS}} \mathbf{T}(\mathbf{u})\cdot\hat{\mathbf{n}}\,\cdot\,\tilde{\mathbf{u}}\;dS \;+\; \int_{\Sigma_{OC}} \mathbf{T}(\mathbf{u})\cdot\hat{\mathbf{n}}\,\cdot\,\tilde{\mathbf{u}}\;dS \;+\; \int_{\Gamma} \mathbf{T}(\mathbf{u})\cdot\hat{\mathbf{n}}\,\cdot\,\tilde{\mathbf{u}}\;dS\;. \tag{44}$$

Upon substituting the expressions of the different tractions given by Eqs. (35), (B.11) and (41) we obtain:

$$\int_{\Sigma} \mathbf{T}(\mathbf{u})\cdot\hat{\mathbf{n}}\,\cdot\,\tilde{\mathbf{u}}\;dS \;=\; \int_{\Sigma_{FS}} \rho\,\ddot{\zeta}\,\tilde{\mathbf{u}}\cdot\hat{\mathbf{n}}\;dS \;-\; \int_{\Sigma_{OC}} \rho_w\,h_w\,(\ddot{\mathbf{u}}\cdot\hat{\mathbf{n}})\,(\tilde{\mathbf{u}}\cdot\hat{\mathbf{n}})\;dS \;+\; \int_{\Gamma} \boldsymbol{\mathcal{D}}_t^W(\mathbf{u}^V_{t'\leq t})\,\cdot\,\tilde{\mathbf{u}}\;dS\;. \tag{45}$$

The weak form (42) must be satisfied by every admissible displacement $\tilde{\mathbf{u}} \in \mathbf{H}^1(V_S)$, where $\mathbf{H}^1(V_S)$ denotes the space of vector fields that, together with their first derivatives, are square-integrable on V_S. It can be shown that the vector fields in $\mathbf{H}^1(V_S)$ are continuous in a weak sense in V_S, which makes $\mathbf{H}^1(V_S)$ a suitable space for describing admissible displacements in the solid. On the contrary, the continuity of traction is a natural property of weak formulations in the sense that it is satisfied implicitly, just as the free surface condition.

2.7.2 Fluid regions

The weak form of the wave equation in the fluid regions is obtained by taking the $L^2(V_F)$ scalar product of each side of Eqs. (21), (20) and (30) with admissible potentials $\tilde{\chi} \in H^1(V_F)$, $\tilde{\zeta} \in H^1(V_F)$ and an admissible vector $\tilde{\mathbf{w}} \in \mathbf{L}^2(V_F)$, respectively, and integrating by parts over V_F to remove the second-order space derivatives, which gives:

$$\int_{V_F} \frac{1}{c^2}\,\ddot{\zeta}\,\tilde{\zeta}\;dV = -\int_{V_F} (\nabla\chi + \zeta\,\mathbf{s} + \mathbf{w})\cdot\nabla\tilde{\zeta}\;dV + \int_{\Sigma_{FS}} (\nabla\chi + \zeta\,\mathbf{s} + \mathbf{w})\cdot\hat{\mathbf{n}}\,\tilde{\zeta}\;dS\;, \tag{46}$$

$$\int_{V_F} \frac{1}{c^2}\,\ddot{\chi}\,\tilde{\chi}\;dV = \int_{V_F} \frac{1}{c^2}\,\Big(\ddot{\zeta} + (\nabla\chi + \mathbf{w})\cdot\mathbf{g} + N^2\,\zeta - \psi(\mathbf{u})\Big)\,\tilde{\chi}\;dV\;, \tag{47}$$

and

$$\int_{V_F} (\dot{\mathbf{w}} + 2\,\boldsymbol{\Omega}\times\mathbf{w})\,\cdot\,\tilde{\mathbf{w}}\;dV = -\int_{V_F} 2\boldsymbol{\Omega}\times(\nabla\chi + \zeta\,\mathbf{s})\,\cdot\,\tilde{\mathbf{w}}\;dV\;. \tag{48}$$

Finally, we enforce the continuity of normal displacement across the fluid-solid interfaces, so that Eq. (46) becomes:

$$\int_{V_F} \frac{1}{c^2}\,\ddot{\zeta}\,\tilde{\zeta}\;dV \;=\; -\int_{V_F} (\nabla\chi + \zeta\,\mathbf{s} + \mathbf{w})\cdot\nabla\tilde{\zeta}\;dV + \int_{\Sigma_{FS}} \mathbf{u}\cdot\hat{\mathbf{n}}\,\tilde{\zeta}\;dS\;. \tag{49}$$

Note that the way we couple the fluid and the solid regions is very similar to the DtN coupling strategy detailed in the previous section. The key issue is again to solve the equation in the solid with a boundary condition in traction and to solve the equation in the fluid with normal displacement imposed on Σ_{FS}. The only difference is semantic: the normal displacement is now a Neumann boundary condition from the fluid side because of the potential decomposition (19). The fluid-solid coupling strategy therefore consists in building a Neumann-to-Dirichlet operator on Σ_{FS}.

In many cases of practical interest, for example in applications involving offshore seismic acquisition in the petroleum industry, we may be interested in a medium in which the fluid layer comprises a free surface (typically the surface of the ocean). In this case, it is worth mentioning that the free-surface condition for the potential formulation we use in the fluid is a Dirichlet condition, not a Neumann condition as in the case of a solid, because the potentials should vanish at the surface to implement zero pressure, as can be deduced from (23) and (24).

2.7.3 Self-gravitation

In order to establish the weak form of Eq. (10), we consider Poisson's equation within the finite volume $\mathcal{B}$. Multiplying with an admissible potential $\tilde{\psi} \in H^1(\mathcal{B})$ and integrating the Laplacian and the divergence terms by parts gives

$$\begin{aligned}\int_{\mathcal{B}} \nabla\psi(\mathbf{u}) \cdot \nabla\tilde{\psi}\; dV - \int_{\partial\mathcal{B}} \nabla\psi(\mathbf{u}) \cdot \hat{\mathbf{n}}\,\tilde{\psi}\; dS \;=& \\ -4\pi G \left\{ \int_{V_S} \rho\,\mathbf{u} \cdot \nabla\tilde{\psi}\; dV - \int_{\partial\mathcal{B}} \rho\,\mathbf{u}\cdot\hat{\mathbf{n}}\,\tilde{\psi}\; dS + \int_{V_F} \rho\;(\nabla\chi + \zeta\,\mathbf{s} + \mathbf{w}) \cdot \nabla\tilde{\psi}\; dV \right\}& \;, \end{aligned} \tag{50}$$

where the jump condition (37) across fluid-solid interfaces is taken into account naturally. Then, upon applying the exterior boundary condition (B.8), we obtain

$$\begin{aligned}\int_{\mathcal{B}} \nabla\psi(\mathbf{u}) \cdot \nabla\tilde{\psi}\; dV - \int_{\partial\mathcal{B}} \mathcal{D}^W(\psi(\mathbf{u}))\,\tilde{\psi}\; dS \;=& \\ -4\pi G \left\{ \int_{V_S} \rho\,\mathbf{u} \cdot \nabla\tilde{\psi}\; dV + \int_{V_F} \rho\;(\nabla\chi + \zeta\,\mathbf{s} + \mathbf{w}) \cdot \nabla\tilde{\psi}\; dV \right\}& \;, \end{aligned} \tag{51}$$

where the DtN operator $\mathcal{D}^W$ is given by (B.6).

3 SPECTRAL-ELEMENT APPROXIMATION

3.1 Spatial discretization

The SEM is based upon a generalized Galerkin approximation (see e.g., Deville et al. 2002, p. 51) of the weak forms (42), (47), (49), (48) and (51), which we outline in this section.

Let h stand for a generic parameter related to the geometrical discretization process, for example the typical size of an element or the distance between two adjacent grid points. The discrete problem can be written as: find $\mathbf{u}_h \in \mathbb{D}_h$, $\zeta_h \in \mathbb{P}_h$, $\chi_h \in \mathbb{P}_h$, $\mathbf{w}_h \in \mathbb{W}_h$ and $\psi_h \in \mathbb{G}_h$ such that $\forall\tilde{\mathbf{u}} \in \mathbb{D}_h$, $\forall\tilde{\zeta} \in \mathbb{P}_h$, $\forall\tilde{\chi} \in \mathbb{P}_h$, $\forall\tilde{\mathbf{w}} \in \mathbb{W}_h$, $\forall\tilde{\psi} \in \mathbb{G}_h$:

$$\begin{aligned}(\rho\,\ddot{\mathbf{u}}_h\,;\,\tilde{\mathbf{u}})_h^S \;+\; (2\rho\,\mathbf{\Omega}\times\dot{\mathbf{u}}_h\,;\,\tilde{\mathbf{u}})_h^S \;+\; \boldsymbol{\mathcal{A}}_h^S(\mathbf{u}_h,\psi_h\,;\,\tilde{\mathbf{u}}) =&\; \boldsymbol{\mathcal{C}}_h^{SF}(\ddot{\zeta}_h\,;\,\tilde{\mathbf{u}}) \;+\; \boldsymbol{\mathcal{C}}_h^{OC}(\ddot{\mathbf{u}}_h\,;\,\tilde{\mathbf{u}}) \\ &+\; \boldsymbol{\mathcal{C}}_h^{\Gamma}(\mathbf{u}_h\,;\,\tilde{\mathbf{u}}) \;+\; (\mathbf{f}_h\,;\,\tilde{\mathbf{u}})_h^S \;,\end{aligned} \tag{52}$$

$$\left(\frac{1}{c^2}\,\ddot{\zeta}_h\,;\,\tilde{\zeta}\right)_h^F \;+\; \boldsymbol{\mathcal{A}}_h^{F,\zeta}(\zeta_h,\chi_h,\mathbf{w}_h\,;\,\tilde{\zeta}) = \;\boldsymbol{\mathcal{C}}_h^{FS}(\mathbf{u}_h\,;\,\tilde{\zeta}) \;, \tag{53}$$

$$\left(\frac{1}{c^2}\,\ddot{\chi}_h\,;\,\tilde{\chi}\right)_h^F \;+\; \boldsymbol{\mathcal{A}}_h^{F,\chi}(\ddot{\zeta}_h,\zeta_h,\chi_h,\mathbf{w}_h\,;\,\tilde{\chi}) = \;0 \;, \tag{54}$$

$$(\dot{\mathbf{w}}_h\,;\,\tilde{\mathbf{w}})_h^F \;+\; \boldsymbol{\mathcal{R}}_h(\zeta_h,\chi_h,\mathbf{w}_h\,;\,\tilde{\mathbf{w}}) = \;\mathbf{0} \;, \tag{55}$$

$$\boldsymbol{\mathcal{P}}_h(\psi_h\,;\,\tilde{\psi}) = \;\boldsymbol{\mathcal{D}}_h(\mathbf{u}_h,\zeta_h,\chi_h,\mathbf{w}_h\,;\,\tilde{\psi}) \;, \tag{56}$$

where $\mathbb{D}_h$, $\mathbb{P}_h$, $\mathbb{W}_h$ and $\mathbb{G}_h$ denote some finite-dimensional subspaces of $\mathbf{H}^1(V_S)$, $H^1(V_F)$, $\mathbf{L}^2(V_F)$ and $H^1(V)$, respectively, and $(\;;\;)_h^S$ (resp. $(\;;\;)_h^F$) stands for an approximate scalar product on $\mathbf{L}^2(V_S)$ (resp. $L^2(V_F)$). $\boldsymbol{\mathcal{A}}_h^S$ results from the approximation of Eq. (7), which involves the elastic-gravitational operator in the solid regions. By analogy, we have denoted $\boldsymbol{\mathcal{A}}_h^{F,\zeta}$ and $\boldsymbol{\mathcal{A}}_h^{F,\chi}$ the result of the approximation of the right-hand sides of Eqs. (47) and (49). Approximate coupling operators defined on the interfaces of the medium are labeled $\boldsymbol{\mathcal{C}}_h$, with a superscript referring to the different boundary terms in Eqs. (45) and (49). $\boldsymbol{\mathcal{R}}_h$ arises from the discretization of the precession equation (48) in the rotating fluid regions. Finally, $\boldsymbol{\mathcal{P}}_h$ refers to the approximation of the left-hand side of the Poisson-Laplace equation (51), while $\boldsymbol{\mathcal{D}}_h$ arises from the discretization of the right-hand side (i.e., the divergence term).

3.1.1 Geometrical approximation and mesh design

The first step of the spatial discretization process is to divide the computational domain into a mesh of E non-overlapping elements:

$$\overline{V} \;=\; \bigcup_{e=1}^{E} \overline{V^e} \;, \tag{57}$$

each of them being obtained from a reference square (in 2D) or cube (in 3D) based on an invertible mapping:

$$V^e \;=\; \boldsymbol{\mathcal{F}}^e\left(\Lambda^d\right) \;, \quad \Lambda = [-1,1] \;, \tag{58}$$

where $d = 2$ or 3 is the spatial dimension.

Note that the choice of elements with tensorized geometries such as quadrangles in 2D and hexahedra in 3D is a characteristic of the SEM that stems from the choice of tensorized polynomial bases, as will be illustrated in Section 3.1.2. Let us mention that one can generalize the SEM in 2D to triangles (Cohen et al. 2001; Giraldoa & Warburton 2005; Bittencourt 2005; Mercerat et al. 2005) based upon the so-called Fekete points (Taylor et al. 2000), and combine triangles and quadrangles within the same 2D mesh (Komatitsch et al. 2001; Pasquetti & Rapetti 2004). In 3D one could use this approach to couple hexahedra with tetrahedra based upon pyramidal transition elements to ensure the geometrical matching between quadrangular and triangular faces. However, it is worth noting that triangular spectral elements are both more expensive and less accurate than quadrangular spectral elements (Komatitsch et al. 2001), therefore their main interest is to allow for more geometrical flexibility during the mesh generation process.

For the sake of simplicity, we will hereafter assume that the mesh is geometrically conforming, i.e., that two neighboring elements share either a single point or an entire edge or face, but not a partial edge.

Except in a few benchmark cases for which analytical transformations exist, each mapping $\boldsymbol{\mathcal{F}}^e$ needs to be approximated, for example based on a polynomial function defined by a set of n_a so-called ‘anchors’ or ‘control nodes’. If $\mathbf{x}^e$ and $\boldsymbol{\zeta}$ denote the respective generic vectors on V^e and Λ^d, this can be written as:

$$\mathbf{x}^e \;=\; \boldsymbol{\mathcal{F}}^e(\boldsymbol{\zeta}) \;\simeq\; \sum_{a=1}^{n_a} N_a(\boldsymbol{\zeta})\mathbf{x}_a^e \;, \tag{59}$$

where N_a are the shape functions of the anchor nodes $\boldsymbol{\zeta}_a$ (with by definition $N_a(\boldsymbol{\zeta}_b) = \delta_{ab}$) and $\mathbf{x}_a^e = \boldsymbol{\mathcal{F}}^e(\boldsymbol{\zeta}_a)$. In practice, the shape functions are chosen to be linear or quadratic, so that the number of anchors is at most 9 in 2D (see Fig. 2) and 27 in 3D. The reader is referred to Dhatt & Touzot (1984) for detailed formulas defining the shape functions of 2D and 3D elements. Note that because the polynomial order used to approximate the solution of the wave equation in the SEM (see next section) is higher than that defining the shape functions, the mapping is said to be sub-parametric.

The design of a mesh basically consists in choosing the values $\mathbf{x}_a^e$ in Eq. (59) in order to define each spectral element. During this process, it is important to honor the main geological layers and the surfaces across which the material properties of the geological medium are discontinuous. Indeed, as will be seen in Section 3.1.2, density and seismic velocities are approximated by smooth functions inside each element, which means that sharp local variations in the geological medium such as an interface between two layers can only be accounted for at element boundaries. Note also that because the interfaces are approximated based upon element-wise polynomials following Eq. (59), the number of elements must be chosen large enough to correctly describe the variations of topography and of the shape of the interfaces.

At the scale of the full Earth, topography is defined as a small and smooth variation with respect to a spherical or ellipsoidal reference. One must therefore first define a mesh of hexahedra that is suitable for a sphere or an ellipsoid. A classical way of proceeding is to tile the spherical (or ellipsoidal) interfaces based upon the so-called ‘cubed sphere’ analytical transformation (e.g., Sadourny 1972; Ronchi et al. 1996). This mapping, which consists in a central projection of the six faces of a cube onto its circumscribed sphere, provides a mesh with quasi-uniform grid sampling, as illustrated in Fig. 3. Once the different interfaces have been meshed with a set of quadrangles, they are connected in the radial direction to define a mesh of hexahedra. In order to circumvent the singularity at the center of the sphere, a cube is used instead inside the inner core, as shown in Fig. 4. The reader is referred to Chaljub et al. (2003) for the analytical expression defining the transition from the sphere to this central cube.

A proper mesh should be relatively regular, i.e., the seismic wavelengths should be sampled relatively uniformly throughout the medium. The motivation is twofold: first, oversampling the wavelengths would result in unnecessary calculations and memory storage from a computational point of view, and second, small grid elements would penalize the choice of the time step used in the explicit time-marching scheme because of the Courant-Friedrichs-Lewy (CFL) stability criterion (see Section 4).

The mesh shown in Fig. 4 does not satisfy this regularity property because the process of embedding spherical interfaces makes the lateral grid size decrease linearly with depth, while seismic velocities usually increase with depth. For geometrical reasons, the resulting number of grid points per P-wavelength in such a grid would be about eight times greater in the inner core than in the crust. The same problem arises when studying the response of sedimentary basins, because there is typically at least a factor of 5 between the values of seismic velocities in the bedrock and in the sediments. To overcome this issue, the mesh must be coarsened with depth, either directly at the contact between two layers of elements, or over a few layers of elements in the radial direction. In the first case, geometrical conformity is lost, and one faces the difficulty of matching solutions defined on non-matching sub-grids. The second case is easier to handle in the sense that the implementation of the continuity conditions between elements is unchanged, the only issue being that the mesh becomes geometrically non-structured (which means that the number of elements that share a given grid point, i.e., the valence of that grid point, can in principle become arbitrarily large). For more details, the reader can refer to Chaljub et al. (2003) for an example of a non-conforming implementation of the SEM and to Komatitsch & Tromp (1999, 2002a) for examples of conforming implementations on non-structured grids.

Once a spectral-element code has been written (following the principles detailed in the next sections), in many cases of practical interest mesh design is going to be the most critical and time-consuming task before being able to run an accurate simulation. This task is difficult because the use of hexahedra as elementary mesh elements is not always convenient to capture geological features (in classical finite-element methods, one usually has the flexibility of using tetrahedra, pyramids and prisms in addition to hexahedra). For example when discretizing basin edges in site effect studies, on the one hand one wants to have elements lying on the interface between the bedrock and the sediments in order to properly account for the mechanical contrast, but on the other hand, the deformation within the elements must be kept reasonably small for accuracy purposes. A trade-off can be found by defining an ad-hoc depth below which the interface is properly accounted for, while it is only approximated at shallower depths (e.g., see Komatitsch et al. 2004, and Section 6.1). What this example suggests is that in the SEM mesh design is always a difficult step that requires expertise and trial-and-error, and that usually cannot be fully automated. Let us mention however that the field of hexahedral mesh generation has significantly evolved in the last few years. Powerful mesh generation packages (also known as ‘meshers’) are now available, for instance CUBIT by SANDIA National Laboratories, which is based upon powerful mesh creation algorithms (Knupp 1999; Tautges 2004). The use of such packages greatly simplifies mesh design for complex 3D models.

3.1.2 Functional approximation

Based upon the set of spectral elements defined above, we approximate admissible displacements and potentials by continuous piecewise polynomials defined on the reference domain Λ^d and transported through the local mappings (58). This can be written as:

$$\mathbb{D}_h = \left\{ \tilde{\mathbf{u}} \in \left(\mathcal{C}^0(V_S)\right)^d, \quad \tilde{\mathbf{u}}^e \in \left(\mathbb{Q}_N(\Lambda^d)\right)^d \quad \forall e = 1,\ldots,E_S \right\} , \tag{60}$$

$$\mathbb{P}_h = \left\{ \tilde{\phi} \in \mathcal{C}^0(V_F), \quad \tilde{\phi}^e \in \mathbb{Q}_N(\Lambda^d) \quad \forall e = 1,\ldots,E_F \right\} , \tag{61}$$

$$\mathbb{G}_h = \left\{ \tilde{\psi} \in \mathcal{C}^0(V), \quad \tilde{\psi}^e \in \mathbb{Q}_N(\Lambda^d) \quad \forall e = 1,\ldots,E \right\} , \tag{62}$$

where E_S and E_F stand for the number of elements in the solid and fluid regions, respectively. The superscript indicates a composition with the local mapping: for example, $\tilde{\mathbf{u}}^e$ is defined on the reference domain by $\tilde{\mathbf{u}}^e = \tilde{\mathbf{u}}_{|V^e} \circ \boldsymbol{\mathcal{F}}^e$. The space of continuous scalar fields on W (which stands for either V, V_S or V_F) is denoted $\mathcal{C}^0(W)$, and $\mathbb{Q}_N(\Lambda^d)$ is the space of polynomials of order at most N in each direction of space. In applications of the SEM to wave propagation problems, N is typically selected between 4 and 8 (see section 5.1 for more details). Here we have assumed that the same order was used for all directions, but this is not a constraint imposed by the method. However, in practice the mesh is often non structured, i.e., the elements are not regularly distributed along X, Y and Z, and the three directions are therefore coupled in the mesh, which implies that the same polynomial order must indeed be used for all directions.

The space of admissible precession vectors is discretized in the same way, except that the continuity requirement does not hold anymore:

$$\mathbb{W}_h = \left\{ \tilde{\mathbf{w}} \in \mathbf{L}^2(V_F), \quad \tilde{\mathbf{w}}^e \in \left(\mathbb{Q}_N(\Lambda^d)\right)^d \quad \forall e = 1,\ldots,E_F \right\} . \tag{63}$$

To make these definitions complete, a basis of $\mathbb{Q}_N(\Lambda^d)$ must be provided, and this is where tensorization arises. We start by introducing the set of Gauss-Lobatto-Legendre (GLL) points (e.g., Canuto et al. 1988), which are by convention defined on the reference interval $\Lambda = [-1, 1]$ as the $(N + 1)$ zeroes of the polynomial of order N $Q(\xi) = (1 - \xi^2)L'_N(\xi)$, where L'_N is the derivative of the Legendre polynomial of order N on Λ:

$$Q(\xi_i^N) = 0 \quad \forall\, i = 0,\ldots,N. \tag{64}$$

Note that we choose the GLL points because they include the extremities of the reference interval, which will ease the implementation of continuity conditions between elements. Next, we define a basis of $\mathbb{Q}_N(\Lambda)$ by considering the Lagrange interpolants at the GLL points (Figure 5), i.e., the $N + 1$ polynomials of order N that satisfy

$$h_i^N(\xi_j^N) \;=\; \delta_{ij}, \quad \forall\,(i,j) = \{0,\ldots,N\}^2, \tag{65}$$

where δ_{ij} is the Kronecker delta symbol. As mentioned previously, the polynomial basis on the reference domain Λ^d is obtained by tensorization of these 1D bases. Let $\boldsymbol{\Xi}^d$ be the set of points obtained by tensorization of the GLL points (Figure 6). Assuming that we are in 3D (i.e., $d = 3$), the points of $\boldsymbol{\Xi}^d$ are defined as $\boldsymbol{\zeta}_{ijk}^N \;=\; (\xi_i^N, \xi_j^N, \xi_k^N)$ and the associated Lagrange interpolants are $h_{ijk}^N(\boldsymbol{\zeta}) \;=\; h_i^N(\xi)\, h_j^N(\eta)\, h_k^N(\gamma)$, where $\boldsymbol{\zeta} = (\xi, \eta, \gamma)$ is the generic coordinate vector on the reference cube.

Let for example $\tilde{\mathbf{u}} \in \mathbb{D}_h$ be a discrete displacement vector and let $\mathbf{x} = \boldsymbol{\mathcal{F}}^e(\boldsymbol{\zeta}) \in V_S^e$. For each component $\alpha = 1,\ldots,d$

we can write

$$\tilde{u}_\alpha(\mathbf{x}) \;=\; \tilde{u}^e_\alpha(\boldsymbol{\zeta}) \;=\; \sum_{i=0}^{N}\sum_{j=0}^{N}\sum_{k=0}^{N} \tilde{u}^e_\alpha(\boldsymbol{\zeta}^N_{ijk})\, h^N_{ijk}(\boldsymbol{\zeta}) \;=\; \sum_{i=0}^{N}\sum_{j=0}^{N}\sum_{k=0}^{N} \tilde{u}_\alpha(\mathbf{x}^{e,N}_{ijk})\, h^N_{ijk}(\boldsymbol{\zeta}) \;, \tag{66}$$

where we have introduced the collocation points $\mathbf{x}^{e,N}_{ijk}$ defined by $\mathbf{x}^{e,N}_{ijk} = \boldsymbol{\mathcal{F}}^e(\boldsymbol{\zeta}^N_{ijk})$. Note that the interpolation formula (66) can handle local continuous variations of the elastic parameters inside the elements.

In order to build continuous bases for the displacements and potentials, it is customary to set up a global numbering of the collocation points over the whole domain. We first introduce the number of local collocation points $\mathcal{N}_L = E \times (N+1)^d$, where the subscript L refers to the fact that only a numbering local to the elements is needed. We then obtain the number of global grid points in the entire mesh, $\mathcal{N}_G$, by counting only once the points that belong to several elements. Efficient mesh numbering algorithms are available for this purpose from the finite-element community. Let us consider for example a grid point with local coordinates (i, j, k) on the e-th element, its global index $n \in \{1, \ldots, \mathcal{N}_G\}$ is defined formally as the surjective function $n = n(e, i, j, k)$. We then build a continuous basis of polynomials by considering shape functions $\phi_n(\mathbf{x})$ that we define as follows: if the grid point is interior to an element then $\phi_n(\mathbf{x})$ is defined on V^e by $\phi_n(\mathbf{x}) = h^N_{ijk}(\boldsymbol{\zeta})$ and ϕ_n vanishes outside V^e. If the grid point is shared with the face, edge or corner of another element, say $n = n(e, i, j, k) = n(e', i', j', k')$, then $\phi_n(\mathbf{x})$ is extrapolated to $V^{e'}$ by $\phi_n(\mathbf{x}) = h^N_{i'j'k'}(\boldsymbol{\zeta})$. We can then assign to any discrete displacement field $\tilde{\mathbf{u}} \in \mathbb{D}_h$ a local vector $\tilde{\mathbf{U}}_L$ of dimension $d \times \mathcal{N}_L$ and a global vector $\tilde{\mathbf{U}}_G$ of dimension $d \times \mathcal{N}_G$ (see Deville et al. (2002) for details). Both vectors store the values of the components of $\tilde{\mathbf{u}}$ at the collocation points. The scatter operation that allows one to form the local vector from the global vector involves a rectangular Boolean connectivity matrix, $\mathbf{Q}$, and can be written $\tilde{\mathbf{U}}_L = \mathbf{Q}\,\tilde{\mathbf{U}}_G$. The transpose operation, i.e., the action of $\mathbf{Q}^T$, is a gather process that consists in summing the entries of the local vector into the global vector. The successive action of $\mathbf{Q}^T$ and $\mathbf{Q}$ is referred to as the assembly process, or direct stiffness summation, in the finite-element literature.

3.1.3 Numerical integration

After discretization, the integrals that appear in the weak form of the equation of motion must be evaluated numerically. The choice made in the SEM is to use the GLL collocation points to perform this task. Let q be a function defined on the reference interval Λ, then the integral of q is approximated by

$$\int_\Lambda q(\xi)\, d\xi \;\simeq\; \sum_{i=0}^{N} \omega^N_i\, q(\xi^N_i) \;, \tag{67}$$

where the weights ω^N_i are the integrals of the Lagrange interpolants at the GLL points: $\omega^N_i = \int_\Lambda h^N_i\, d\xi$. This quadrature formula is exact for polynomials of order up to $2N-1$ (see e.g., Funaro 1992).

The quadrature in a space of higher dimension (also known as cubature) is obtained in the SEM by a tensorization process, which is the main reason why we chose to restrict ourselves to quadrangles rather than triangles in 2D, and to hexahedra rather than tetrahedra in 3D. If q is a function defined on the reference domain Λ^d, its integral is approximated by:

$$\int_{\Lambda^d} q(\boldsymbol{\zeta})\, \mathbf{d}\boldsymbol{\zeta} \;\simeq\; \sum_{i=0}^{N}\sum_{j=0}^{N}\sum_{k=0}^{N} \omega^N_i\, \omega^N_j\, \omega^N_k\; q(\xi^N_{ijk}) \;. \tag{68}$$

An important consequence of choosing the integration points to be the collocation points is that the mass matrix, i.e., the matrix representation of the L^2 scalar product, is exactly diagonal. Because this is a key property of the SEM for wave propagation problems, let us briefly recall the proof. Let $n = n(e, i, j, k)$ and $n' = n(e', i', j', k')$ denote two global indices, we define the components of the scalar mass matrix M as

$$M_{nn'} \;=\; \int_V \phi_n(\mathbf{x})\phi_{n'}(\mathbf{x})\; \mathbf{dx} \;, \tag{69}$$

where ϕ_n and $\phi_{n'}$ denote the shape functions introduced in the previous section. The integral is non-zero only if the two grid points belong to at least one common element. Let e denote such an element, and suppose that $n = n(e, i, j, k)$ and $n' = n(e, i', j', k')$. Expressing the integral back on the reference domain gives:

$$M_{nn'} \;=\; \int_{V^e} \phi_n(\mathbf{x})\phi_{n'}(\mathbf{x})\; \mathbf{dx} \;=\; \int_{\Lambda^d} h^N_{ijk}(\boldsymbol{\zeta})\, h^N_{i'j'k'}(\boldsymbol{\zeta}) \mathcal{J}^e(\boldsymbol{\zeta})\, \mathbf{d}\boldsymbol{\zeta} \;, \tag{70}$$

where $\mathcal{J}^e$ is the Jacobian (i.e., the determinant of the Jacobian matrix) of the local mapping (58). Applying the numerical quadrature gives

$$M_{nn'} \;=\; \delta_{ii'}\delta_{jj'}\delta_{kk'}\; \omega^N_i\, \omega^N_j\, \omega^N_k\, \mathcal{J}^e(\xi^N_{ijk}) \;, \tag{71}$$

which is the expected result since the right-hand side is non-zero only for $n' = n$.

3.1.4 System of ordinary differential equations

To finish the discretization process, we expand the generalized Galerkin approximation (52–55) on the polynomial basis using (66) and compute the integrals with the numerical quadrature (68). This gives a system of ordinary differential equations in time that can be written as

$$\mathbf{M}_S\,\ddot{\mathbf{U}}(t) \;+\; \mathbf{Co}\,\dot{\mathbf{U}}(t) = \;\mathbf{K}_S\,\mathbf{U}(t) \;+\; \mathbf{G}\,\boldsymbol{\psi}(t) \;+\; \mathbf{C}^{OC}\,\ddot{\mathbf{U}}(t) \;+\; \mathbf{C}^{SF}\,\ddot{\boldsymbol{\zeta}}(t) \;+\; \mathbf{C}^{\Gamma}\,\mathbf{U}(t) \;+\; \mathbf{F}^{ext}(t)\;, \tag{72}$$

$$\tilde{\mathbf{M}}_F\,\ddot{\boldsymbol{\zeta}}(t) = \;\mathbf{K}_{F,\zeta}\,(\boldsymbol{\zeta},\boldsymbol{\chi},\mathbf{W})\,(t) \;+\; \mathbf{C}^{FS}\,\mathbf{U}(t)\;, \tag{73}$$

$$\tilde{\mathbf{M}}_F\,\ddot{\boldsymbol{\chi}}(t) = \;\mathbf{K}_{F,\chi}\,\left(\ddot{\boldsymbol{\zeta}},\boldsymbol{\zeta},\boldsymbol{\chi},\mathbf{W}\right)(t)\;, \tag{74}$$

$$\mathbf{M}_F\,\dot{\mathbf{W}}(t) = \;\mathbf{R}\,(\boldsymbol{\zeta},\boldsymbol{\chi},\mathbf{W})\,(t)\;, \tag{75}$$

$$\mathbf{P}\,\boldsymbol{\psi}(t) = \;\mathbf{D}\,(\mathbf{U},\boldsymbol{\zeta},\boldsymbol{\chi},\mathbf{W})\,(t)\;, \tag{76}$$

where $\mathbf{U}$, $\boldsymbol{\zeta}$, $\boldsymbol{\chi}$, $\mathbf{W}$ and $\boldsymbol{\psi}$ denote the vectors that store the values of the unknowns at the $\mathcal{N}_G$ global collocation points; $\mathbf{M}_S$ is the mass matrix in the solid, modified to include density; $\mathbf{M}_F$ is the mass matrix in the fluid and $\tilde{\mathbf{M}}_F$ is modified to include the inverse of c^2; $\mathbf{Co}$ is the Coriolis matrix; $\mathbf{K}_S$ and $\mathbf{K}_{F,\zeta}$ are the stiffness matrices in the solid and fluid, respectively; $\mathbf{G}$ is the gradient matrix modified to include density; $\mathbf{C}^{OC}$ is the ocean-crust coupling matrix, $\mathbf{C}^{SF}$ and $\mathbf{C}^{FS}$ are the fluid-solid coupling matrices, and $\mathbf{C}^{\Gamma}$ is the DtN coupling matrix; $\mathbf{R}$ is the precession matrix, $\mathbf{P}$ and $\mathbf{D}$ are the matrix approximations of the Poisson-Laplace and divergence operators and $\mathbf{F}^{ext}$ is the vector of external forces.

It should be noted that none of the above global matrices needs to be explicitly built, because only their action on a vector is needed in order to perform computations. Furthermore, these matrix-vector products can be defined at the elemental level based upon the connectivity matrix $\mathbf{Q}$ introduced in Section 3.1.2. For example, the action of the mass matrix $\mathbf{M}_S$ can be decomposed into $\mathbf{M}_S\,\mathbf{U} = \mathbf{Q}^T\,\mathbf{M}_{S,L}\,\mathbf{U}_L$, where $\mathbf{M}_{S,L}$ is a set of elemental matrices that act on the local vector $\mathbf{U}_L = \mathbf{Q}\,\mathbf{U}$. Note that the coefficients of $\mathbf{M}_{S,L}$ are obtained after multiplying the right-hand side of Eq. (71) by the pointwise values of density.

The reader is referred to Komatitsch & Tromp (1999) for a detailed derivation of the source term $\mathbf{F}_L$ and of the stiffness matrix $\mathbf{K}_{S,L}$ in the absence of gravity. Regarding the effect of the ocean load, note that (45) involves a simple surface integral along the ocean-crust boundary, which shows that in the context of the approximation of Appendix B3 we can efficiently take into account the effects of the oceans represented by the $\mathbf{C}^{OC}$ ocean-crust coupling matrix above by a simple modification of the mass matrix for the degrees of freedom located exactly at the ocean floor.

Finally, let us note that because of the use of a tensorized polynomial basis, the operation count of a product with the elemental stiffness matrix is only $\mathcal{O}(N^{d+1})$ in d dimensions instead of $\mathcal{O}(N^{2d})$ for a full matrix, which is another argument that makes the SEM efficient for 3D calculations.

4 TIME DISCRETIZATION

The system of ordinary differential equations (72–76) is marched in time using a finite-difference scheme. Let us postpone to the end of this section the implementation of rotation, self-gravitation, attenuation and absorbing layers. For the sake of clarity, we write the previous system of differential equations in the compact form:

$$\mathbf{M}\,\ddot{\mathbf{q}}(t) \;=\; \mathbf{F}^{ext}(t) \;-\; \mathbf{F}^{int}(\mathbf{q}) \;-\; \mathbf{F}^{\Sigma}(\mathbf{q}) \tag{77}$$

where $\mathbf{q}$ is a global vector defined as $\mathbf{q} = (\mathbf{U},\boldsymbol{\zeta},\boldsymbol{\chi})^T$. The vector of all internal forces is denoted by $\mathbf{F}^{int}$, and $\mathbf{F}^{\Sigma}$ stands for the surficial forces that result from the action of the coupling operators $\mathbf{C}^{SF}$, $\mathbf{C}^{FS}$ and $\mathbf{C}^{\Gamma}$. As mentioned in the previous section, the ocean-crust coupling term $\mathbf{C}^{OC}$ has been included in the mass matrix $\mathbf{M}$.

4.1 Newmark time stepping method

The Newmark family of integrators (Newmark 1959; Hughes 1987) is written for a given time $t_n = n\Delta t$ as a map $(\mathbf{q}_n, \dot{\mathbf{q}}_n) \rightarrow (\mathbf{q}_{n+1}, \dot{\mathbf{q}}_{n+1})$ that is defined by enforcing the semi-discrete momentum equations at time t_{n+1}:

$$\ddot{\mathbf{q}}_{n+1} = \mathbf{M}^{-1}\left(\mathbf{F}^{ext}_{n+1} - \mathbf{F}^{int}(\mathbf{q}_{n+1}) - \mathbf{F}^{\Sigma}(\mathbf{q}_{n+1})\right)\;, \tag{78}$$

$$\mathbf{q}_{n+1} = \mathbf{q}_n + \Delta t\,\dot{\mathbf{q}}_n + \Delta t^2\left(\left(\frac{1}{2} - \beta\right)\ddot{\mathbf{q}}_n + \beta\,\ddot{\mathbf{q}}_{n+1}\right)\;, \tag{79}$$

$$\dot{\mathbf{q}}_{n+1} = \dot{\mathbf{q}}_n + \Delta t\,\left((1-\gamma)\,\ddot{\mathbf{q}}_n + \gamma\,\ddot{\mathbf{q}}_{n+1}\right)\;, \tag{80}$$

where one needs to select the two parameters $\gamma \in [0,1]$ and $\beta \in [0,1/2]$.

Second-order accuracy (instead of first-order) is obtained if and only if the velocity is updated based upon a centered scheme, i.e., if $\gamma = 1/2$. The particular choice of setting $\beta = 0$ and $\gamma = 1/2$ leads to the explicit central difference method, which is the most widely used in the context of spectral-element simulations of seismic wave propagation. It has the important property of conserving linear and angular momentum and having bounded energy errors (see Hughes (1987) and Kane et al. (2003) for theoretical considerations and Komatitsch & Vilotte (1998) for numerical illustrations of energy conservation). It is conditionally stable, the maximal time step being imposed by the Courant-Friedrichs-Lewy (CFL) (Courant et al. 1928) criterion that states that the speed at which information travels cannot exceed one grid cell per time step. This means that

$$\Delta t \;\leq\; C\,\left(\frac{\Delta x}{\alpha}\right)_{\rm min}\;, \tag{81}$$

where Δx is the distance between adjacent grid points, α is the P-wave speed and C is a constant (typically ranging between 0.3 and 0.5) that depends on the geometry of the mesh and on the spatial dimension of the problem. The order in which operations are performed in the explicit scheme is the following: first, $\mathbf{q}$ (the displacement) is updated from $\dot{\mathbf{q}}$ (the velocity) and $\ddot{\mathbf{q}}$ (the acceleration) at time t_n using (79); second, acceleration at time t_{n+1} is computed by solving (78); finally, velocity is updated based upon the centered formula (80). The only linear system to invert during this process involves the mass matrix, which is exactly diagonal by construction. This is an important argument that favors the Legendre SEM when compared to other spectral methods such as the Chebyshev SEM (see section 5.1).

An alternative formulation of the explicit central-difference method, more adapted to mixed velocity-stress formulations, is to write it in terms of displacement and velocity, provided that the two quantities be staggered in time (Festa & Vilotte 2005). The scheme consists in defining the map $\left(\mathbf{q}_{n-\frac{1}{2}},\dot{\mathbf{q}}_n\right)\rightarrow\left(\mathbf{q}_{n+\frac{1}{2}},\dot{\mathbf{q}}_{n+1}\right)$ based upon the mid-point rule

$$\mathbf{q}_{n+\frac{1}{2}} = \mathbf{q}_{n-\frac{1}{2}} \;+\; \Delta t\;\dot{\mathbf{q}}_n\;, \tag{82}$$

$$\dot{\mathbf{q}}_{n+1} = \dot{\mathbf{q}}_n \;+\; \Delta t\;\mathbf{M}^{-1}\left(\mathbf{F}^{ext}_{n+\frac{1}{2}} - \mathbf{F}^{int}(\mathbf{q}_{n+\frac{1}{2}}) - \mathbf{F}^{\Sigma}(\mathbf{q}_{n+\frac{1}{2}})\right)\;. \tag{83}$$

The slight difference between the two methods is that the mid-point rule evaluates forces at averaged times, whereas the Newmark scheme performs a time-average of the forces.

Finally, let us recall that coupling fluid and solid regions requires exchanging the normal displacement $\mathbf{u}\cdot\hat{\mathbf{n}}$ and the Lagrangian pressure perturbation $(-\rho\,\ddot{\zeta})$ from one side of the fluid-solid interface to the other. This can be done without iterating on the coupling condition because both quantities are known at the same time (through $\mathbf{q}$ and $\ddot{\mathbf{q}}$). As noticed by Chaljub & Valette (2004), this is a consequence of applying the potential decomposition (19) to the displacement instead of velocity. This has important consequences in practice because it greatly simplifies the implementation of the SEM algorithm and reduces the computational cost by completely suppressing iterations.

4.2 Rotation

Taking into account the effects of rotation requires adding the Coriolis force in the solid regions and solving (75) for the precession vector $\mathbf{W}$ in the fluid regions. Note that because the Coriolis force involves velocity, in principle this term should be treated based upon an implicit time-marching scheme. However, because the Coriolis effect matters mostly at very long period (e.g., Dahlen & Tromp 1998), in practice it is acceptable to purposely lose the second-order accuracy of the time-stepping method for the Coriolis term by handling it based upon an explicit scheme (Komatitsch & Tromp 2002b) because the time step used is always very small compared to the periods involved. Likewise, the precession equation in the fluid regions can be solved based upon a simple first-order Euler scheme.

In Figure 7, we show the effect of the Coriolis forcing on the frequencies of two eigenmodes of the Earth: the so-called football mode ${}_0S_2$ and the recently detected ${}_2S_1$ mode that involves the motion of the entire core (Rosat et al. 2003). The spectra have been obtained by post-processing a spectral-element time series recorded at an epicentral distance of 90° of a point double-couple source in the PREM reference Earth model (Dziewonski & Anderson 1981) without the ocean layer. Note that only the Coriolis forcing term has been included in the spectral-element calculations. Other effects of the rotation of the Earth (centrifugal potential, ellipticity) have been ignored. Because we needed a long time series to compute the spectra (about 100 hours), we also neglected the redistribution of mass to get results in a reasonable amount of compute time.

The effect of rotation is to split the degenerate eigenfrequencies ${}_n\omega_l$ of the spherically-symmetric model into $2l+1$ singlets, which are visible on the plots. Also shown on Figure 7 are the predictions of a first-order splitting theory (see e.g., Dahlen & Tromp 1998, p. 605). The difference with the apparent eigenfrequencies derived from the spectral-element synthetic seismograms illustrates the magnitude of higher-order effects in the Coriolis splitting.

4.3 Self-gravitation

Taking into account the perturbation of the gravitational potential does not affect the accuracy of the time-stepping method but reduces its efficiency because the algebraic system (76) must be solved at each time step. Because the Poisson-Laplace matrix $\mathbf{P}$ is symmetric, the system can be solved for instance based on a conjugate gradient (CG) method, the efficiency of which is governed by the condition number κ of the matrix (i.e., the ratio between the largest and the smallest of its eigenvalues). The number of CG iterations needed to reach a given level of accuracy scales as the square root of κ. Unfortunately, the Poisson-Laplace matrix arising from the spectral-element discretization is known for being poorly conditioned (see e.g., Deville et al. 2002). A diagonal preconditioner is used by Chaljub & Valette (2004) but results in poor numerical efficiency (a number of iterations ranging between 50 and 100 is needed to obtain an acceptable level of accuracy). Additional work is therefore needed to build an efficient preconditioner and to be able to include the redistribution of mass in routine calculations.

4.4 Attenuation

Including the effects of attenuation requires marching the memory variables in time according to Eq. (A.7). This can be achieved based upon a fourth-order Runge-Kutta method (see e.g., Komatitsch & Tromp 1999, and references therein). Once the memory variables are updated, the stress tensor is given by Hooke's law (A.6), and the internal forces can be computed.

In global seismology, bulk attenuation is often ignored because Q_κ is typically one order of magnitude greater than Q_μ. Note that a complete treatment of attenuation should in principle include fluid regions, which implies that the potential formulation (19) should be modified to include appropriate memory variables. However, in global seismology, attenuation in the fluid is almost always completely negligible (e.g., Dahlen & Tromp 1998).

4.5 Implementation of a Perfectly Matched Layer

As mentioned in Appendix (A2), a Perfectly Matched Layer (PML) absorbing region for the seismic wave equation is naturally formulated in terms of velocity and stress, i.e., for a system of first-order equations in time (e.g., Collino & Tsogka 2001). In recent years, efforts have been made to derive PML formulations suitable for the seismic wave equation written as a second-order system in displacement (e.g., Komatitsch & Tromp 2003; Basu & Chopra 2003, 2004; Festa & Vilotte 2005). To our knowledge, so far two of these approaches have been employed to adapt the PML to the SEM, which is based on the second-order system in displacement: Komatitsch & Tromp (2003) derived a formulation of the PML that is directly adapted to second-order equations, and Festa & Vilotte (2005) showed that the classical first-order PML formulation could be used as is, based upon a discrete equivalence between the Newmark time-stepping method and the mid-point rule applied to a staggered velocity-stress approximation of Eqs. (A.13) and (A.14). An alternative is to adapt the SEM to the PML by constructing a SEM formulation based on the mixed velocity-stress system, which is well adapted to the introduction of PML (Cohen & Fauqueux 2005).

Both formulations are equivalent in the sense that they are equally efficient for absorbing body and surface waves and that they suffer from the same drawbacks as the original method: i.e., difficulties to absorb waves at grazing incidence (Collino & Monk 1998; Winton & Rappaport 2000) and intrinsic instabilities in some anisotropic media (Bécache et al. 2003). However, while Komatitsch & Tromp (2003) obtain a system of third-order equations in time (which is further decomposed into a second-order system plus a first-order equation solved by an additional Runge-Kutta scheme), the formulation of Festa & Vilotte (2005) fits naturally in the context of the Newmark scheme and can therefore be more easily added to existing spectral-element algorithms without major modifications of the time-stepping scheme.

5 IMPLEMENTATION

5.1 Choice of parameters for accurate calculations

In a standard FEM, low-order polynomials (usually of order 1 or 2) are used to discretize functions, and therefore the accuracy of the method is mainly governed by the typical size of an element in the mesh, h. In a SEM, however, high-order Lagrange interpolants are used to express functions. Therefore, one can use the polynomial order N chosen to represent functions on an element as an additional parameter to control the accuracy of the method.

The GLL numerical integration rule is exact only for polynomials of order $2N-1$ (e.g., Canuto et al. 1988). This implies that because it involves the product of two polynomials of order N, the displacement and the test function, integration on the reference element is never exact, even in the simplest case of a reference cube with homogeneous material properties. For deformed and/or heterogeneous elements, there are additional errors related to curvature (Maday

& Rønquist 1990). Thus in the Legendre SEM we obtain a diagonal mass matrix by purposely selecting a numerical integration rule that is not exact (but of course still very accurate) for the polynomial basis chosen (in the finite-element literature, such a choice is known as sub-integration). A different choice is made in the Chebyshev SEM used by some authors (e.g., Priolo et al. 1994; Seriani 1998), in which an integration rule that is exact for the polynomial basis chosen is used, with the consequence that the mass matrix is no longer diagonal.

To our knowledge, no theoretical analysis of the accuracy of the SEM for elastic media is available in the literature, and only Tordjman (1995) and Cohen & Fauqueux (2000) have attempted such a theoretical accuracy study for the SEM in the acoustic case, and Seriani & Priolo (1994) have addressed the issue based on a numerical study, also in the acoustic case. Because of the lack of such theoretical criteria, we use heuristic rules in order to select the polynomial order to use in practice for an elastic SEM with a non-regular deformed mesh and a heterogeneous medium. These rules of thumb have been developed over the years by trial and error based upon a large number of numerical tests for which a quasi-analytical reference solution was known. In particular, we have used the main conclusions of Seriani & Priolo (1994) in the acoustic case and checked numerically for simple cases that these conclusions extend reasonably well to the elastic case. Based on these numerical experiments, we observe that if one uses a polynomial order lower than typically 4, one looses the advantages of using a SEM, because the calculations lead to a large amount of numerical dispersion, i.e., to similar inaccuracies as with standard FEMs (Marfurt 1984). On the contrary, if one selects a very large polynomial order, e.g., greater than 10, the SEM is spatially very accurate, but the computational requirements become prohibitive because of the size of the calculations related to matrix multiplications involving the full stiffness matrix, a process with a cost of $O(N^4)$ in 3D, i.e., the numerical cost of the technique becomes very high. Let us also recall that the GLL numerical integration points are non-evenly spaced and that in the case of a high order they become clustered toward the edges of each spectral element (e.g., Canuto et al. 1988). More precisely, one can show that the spacing between the first two GLL points of the reference interval varies approximately as $O(N^{-2})$, and as a result of the small distance between these first two points, very small time steps have to be used to keep the explicit time-marching scheme stable (see Section 4), which drastically increases the cost of the Legendre SEM. Therefore, the empirical conclusion is that for most seismic wave propagation problems, polynomial orders between approximately 4 and 10 should be used in practice. In our numerical simulations, we often use a polynomial order $N = 4$. In order to obtain accurate results, we use another heuristic rule of thumb that says that for this polynomial order the average grid spacing h should be chosen such that the average number of points per minimum wavelength $\lambda_{\min}$ in an element, $(N+1)\lambda_{\min}/h$, be roughly equal to 5. Note that this value is of the same order as that obtained in the context of high-order finite-difference methods applied to wave propagation problems.

5.2 Parallel implementation

Section 3.1.1 explained the basic concepts of mesh design in the SEM. However, real meshes designed to study large 3D models are usually too large to fit on a single computer in terms of memory. One then needs to turn to parallel machines, for instance clusters of personal computers or grids of computers, which all have a distributed memory architecture. In order to program such parallel machines, one needs to use a message-passing methodology, usually based upon a library called MPI (e.g., Gropp et al. 1994), an acronym for 'Message Passing Interface', which has the advantage of being freely available on most computer systems and therefore very portable.

Let us mention that the SEM can efficiently run on high-latency networks such as clusters or grids of computers because it is relatively insensitive to the speed of the network connecting the different processors. The main reason for that is that we can use a fully explicit time-marching scheme (see Section 4). In such schemes, one mostly needs to perform small local matrix-vector products in each spectral element, and as a consequence the processors spend most of their time doing actual calculations, and only a small amount of time exchanging information, which means that the algorithm is not very sensitive to the communication speed.

Once a mesh has been created, it needs to be split into slices if one wants to run the SEM on a parallel computer. Powerful algorithms called 'mesh partitioners' are available for this purpose, such as METIS, which is a set of programs for partitioning graphs and finite-element meshes. The algorithms implemented in METIS are based on sophisticated multilevel graph-partitioning schemes (Karypis & Kumar 1998a,b). The mesh should be decomposed into as many slices as the number of processors one plans to use on the machine. Calculations can then be performed locally by each processor on the spectral elements that constitute the mesh slice it carries after the mesh partitioning step. In the time-marching algorithm, one communication phase is then required at each time step in order to sum the internal forces computed at the common faces, edges, and corners shared by mesh slices carried by different processors. MPI communications are performed based upon a (constant) communication topology produced once and for all by the mesh partitioner. This topology represents the sequence of messages that needs to be exchanged between the slices at each time step. It is constant because there is no dynamic (i.e., adaptive) remeshing in the SEM applied to seismic wave propagation studies, which are small perturbation problems for which a constant mesh is sufficient.

6 APPLICATIONS

6.1 3D ground motion in alpine valleys

As a first example of the application of the SEM to realistic wave propagation problems, we consider the simulation of ground motion in the alpine valley of Grenoble, French Alps, France. Like sedimentary basins, alpine valleys are known for producing strong site effects because of (i) stiff bedrock conditions leading to large impedance contrasts between bedrock and sediments and (ii) thick post-glacial deposits of lacustrine and fluviatile sediments. The computation of site effects in alpine valleys has received considerable attention since the pioneering work of Bard & Bouchon (1980a,b). It is out of the scope of this article to review all the studies and methods devoted to this topic. Let us mention however that most of these studies are restricted to two-dimensional geometries. The computation of 3D seismic wave propagation in alpine valleys is challenging for two reasons: first, unlike in large sedimentary basins, seismic energy diffracted off the valley edges and transported by surface waves dominates the seismic signal (e.g., Cornou et al. 2003) and is hardly separable from body wave reflections. Second, alpine valleys are often deeply embanked and exhibit strong topographic variations of the free surface and of the interface between sediments and bedrock. With its ability to handle 3D geometries and its accuracy regarding the computation of surface waves, the SEM is therefore well suited to simulate wave propagation in alpine valleys.

We consider the city of Grenoble in the French Alps. Fig. 8 shows the 'Y' shape of the valley, surrounded by three topographic units with a typical elevation of 1000 m to 1500 m on the western side (Vercors and Chartreuse massifs) and 2500 m to 3000 m on the eastern side (Belledonne chain). Fig. 8 also displays the surface of the spectral-element mesh used to propagate seismic waves at frequencies up to 1 Hz, assuming a minimal shear wave velocity of 300 $\mathrm{m.s^{-1}}$ in the sediments. The 3D mesh shown in Fig. 9 honors the sediment/bedrock interface, which is well constrained by the inversion of gravimetric anomalies performed by Vallon (1999). As explained in section 3.1.1, it is difficult to honor the interface near the edges of the valley because (i) this requires the use of a fully 3D mesh generator and (ii) even with such a tool, the elements located near the edges are expected to be strongly distorted, thus leading to a loss of accuracy. Here we avoid this difficulty by defining a threshold depth above which the interface is not honored but rather interpolated within the spectral elements (see Fig. 9), as suggested by Komatitsch et al. (2004). This solution is not fully satisfactory because at shallow depths (in particular near valley edges) the contrast between bedrock and sediments is smeared out due to the use of high-order ($N = 4$) polynomial interpolation within each spectral element.

We choose to simulate the April 26, 2003 $M_L = 2.9$ Lancey event, which occurred on the Belledonne border fault less than 10 km from the valley edges (Thouvenot et al. 2003). Based upon measurements performed in a 550 m-deep borehole (Nicoud et al. 2002), the velocity model used in the sediments is defined as:

$$\left\{ \begin{array}{lcl} \beta & = & 300.0 \ + \ 19.0\sqrt{d} \ , \\ \alpha & = & 1450.0 \ + \ 1.2\, d \ , \end{array} \right. \tag{84}$$

in which d is depth in m, α and β are the P and S velocities in $\mathrm{m.s^{-1}}$, and mass density in $\mathrm{kg.m^{-3}}$ is defined by $\rho = 2140.0 \ + \ 0.125\, d$. Attenuation is taken into account by defining a constant shear quality factor $Q_S = 50$ in the sediments. The bedrock model is adapted from that used by Thouvenot et al. (2003), with P and S velocities in the uppermost layer equal to $\alpha = 5600$ $\mathrm{m.s^{-1}}$ and $\beta = 3200$ $\mathrm{m.s^{-1}}$, respectively. We use a polynomial order $N = 4$ (i.e., $(N+1)^3 = 125$ GLL points per spectral element) in the SEM, which yields a total of approximately 3.3 million grid points and about 10 millions of degrees of freedom.

The time evolution of synthetic vertical ground velocity is represented in Fig. 10. The calculation is accurate up to approximately 1 Hz, and the source we use does not contain energy above this cutoff limit. The source mechanism, a strike-slip event with almost vertical dip, is clearly seen in the first second of the recorded signals. In the next four seconds, one sees the distortion of P and S wavefronts by the low velocities in the sediments. Surface waves generated at the edges of the valley can be observed relatively early (from 3.5 s on) and tend to form planar features aligned with the borders (e.g., between 7.5 s and 8.5 s). The rest of the simulation shows the trapping of energy within the sediments, causing the progressive illumination of the whole basin structure. Note how the wave field becomes complex after only a dozen of seconds of propagation, due to multiple reflections of surface waves diffracted off the valley edges. To give an idea of the typical numerical cost of such a simulation, the calculations required about one gigabyte of memory, and took (in 2004) about 16 hours of CPU time on four 3 GHz Intel Xeon processors to run 60000 time steps of 1 ms each.

Time series of ground velocity recorded at two sites with different soil conditions are displayed in Fig. 11. The source time function used is a smoothed version of a Heaviside step (in practice an error function with a short rise time $\tau = 0.01$

s). The synthetic seismograms are further bandpass-filtered between 0.1 Hz and 2 Hz. The reason why we can analyze frequencies higher than the limit used to design the mesh (1 Hz) is that the signal is dominated by surface waves that at low frequency are sensitive to the velocity model at depth, were velocity increases, and therefore travel at a velocity higher (typically about 600 $\mathrm{m.s}^{-1}$ at 2 Hz) than the minimal S wave velocity in the model, which is found at the surface. The comparison shows a strong amplification (by about a factor of 10) and an increase in duration between the signal recorded in the sediments and on the rock site.

Comparison to data (Chaljub et al. 2005) shows a reasonable agreement for frequencies smaller than 1 Hz, confirming that the long-wavelength structure of the basin is well constrained. The perspective is now to better understand the variability of ground motion observed in high-frequency data (i.e., from 1 Hz to 10 Hz). The small size of the model, allowing computations up to 4 Hz to be performed with accessible computing facilities will help us to address this problem with the SEM.

6.2 3D spectral-element reference solution

One of the goals of seismologists is to constrain the physical properties of the Earth's interior by solving the inverse problem of finding Earth models for which synthetic seismograms match the observations. Most of the methods developed to solve the inverse problem involve the computation of a large number of synthetic seismograms, and different approximations have been derived to produce them in a reasonable amount of CPU time. These methods provide accurate results as long as they are used within their domain of validity, a condition unfortunately not always met in practice. A precise series of tests should therefore be performed to assess the effects of such approximations, but so far these have rarely been conducted due to the lack of an independent solution to compare with (Clévédé et al. 2000).

The application of the SEM to global seismology offers the possibility of overcoming this difficulty by providing a three-dimensional reference solution. As an example, let us show a comparison between the SEM and two methods widely used in global tomography: the Path Average Approximation (PAVA) (Woodhouse & Dziewonski 1984) and Non-linear Asymptotic Coupling Theory (NACT) (Li & Tanimoto 1993; Li & Romanowicz 1995). Both methods are based on perturbation theory around a spherical reference Earth model. The reference solution, expanded on the basis of normal modes, is perturbed to the first order based on the Born approximation to obtain an approximate solution in the 3D model. The solution is thus only valid for 'weak' and smooth-enough 3D heterogeneities. In addition to the Born approximation, PAVA and NACT use the great-circle approximation, in which only 3D heterogeneities lying under the great circle between the source and the receiver are taken into account. This approximation is valid when the wavelength of the model is much larger than the wavelength of the displacement field, i.e., for 'smooth-enough' models. Compared to NACT, PAVA makes the additional approximation that the coupling between dispersion branches is not accounted for in the perturbation. This results in a 1D sensitivity kernel: the effect of an heterogeneity at a given depth does not depend on the position along the great circle. While this is acceptable for Love and Rayleigh waves, such an approximation cannot account for the ray-like sensitivity of body waves. We therefore expect NACT to give a more precise result than PAVA in a 3D model, especially for higher modes.

Fig. 12 shows an example of long-period (100 s and above) synthetic seismograms computed with PAVA, NACT and SEM in the tomographic model SAW24B16 (Mégnin & Romanowicz 2000). The SEM synthetic seismograms are computed on a grid of 1782 spectral elements with 54936 collocation points, and the time step used is 1 s. The comparison of differential seismograms (defined as the difference between 3D and 1D synthetic seismograms) shows that both PAVA and NACT predictions are accurate for the Rayleigh wave R1, but only NACT retrieves the waveforms of higher modes, such as the X wave (Jobert et al. 1977). Note that none of the results perfectly match the spectral-element solution, which is consistent with the approximations used in each method.

Another example in which a spectral-element calculation proved useful can be found in Favier et al. (2004), where a new sensitivity kernel to invert splitting measurements in anisotropic media is proposed, which includes the middle- and near-field terms of the Green's tensor generally neglected in classical theories. Using the spectral-element solution as a reference, the authors assessed the domain of validity of their new kernel and the error made by using classical far-field kernels.

6.3 3D modeling in the D$''$ region

Another application of the SEM is to assess the quality of current tomographic models by providing an independent measure of their ability to fit the data. For example Komatitsch et al. (2002) compute synthetic seismograms using tomographic mantle model S20RTS (Ritsema et al. 1999) and crustal model CRUST2.0 (Bassin et al. 2000). They show that this 3D model explains body-wave travel times for periods up to approximately 20 s but that surface wave dispersion is not accurately accounted for at periods shorter than 40 s.

Here we show a similar comparison between data and synthetic seismograms obtained by coupling the SEM to a normal-mode solution, and we focus our attention on the D$''$ region. This region at the base of the Earth's mantle is known for being very heterogeneous and for significantly affecting the travel times and amplitudes of seismic waves, in particular those diffracted by the core-mantle boundary (CMB). We simulate the September 4, 1997, 621-km deep Fiji event ($M_w = 6.8$) using the PREM model everywhere except in a 370-km thick layer above the CMB (D$''$ region) in which we replace it by the 3D tomographic S-velocity model SAW24B16 (Mégnin & Romanowicz 2000). Perturbations in P-wave velocity and density are obtained from S-wave values by the linear scaling rules $\delta\alpha = 0.40\,\delta\beta$ and $\delta\rho = 0.25\,\delta\beta$ (Kumazawa & Anderson 1969). The spectral-element solution is computed in D$''$ and coupled to two normal-mode solutions in the mantle and core, respectively. The spectral-element mesh used contains about 12000 elements, which corresponds to approximately 4 million grid points. This allows us to compute accurate synthetic seismograms for periods greater than about 12 s. Note that at these periods, using the SEM in the whole model would require us to run on a large parallel computer (Komatitsch et al. 2003), but because of the coupling with the normal-mode solution, the simulation only requires 13 gigabytes of computer memory and runs in less than a day on a cluster of 64 processors (Capdeville et al. 2003b).

Fig. 13 displays the ten stations at which we compare synthetic seismograms to data. These stations are taken from the following networks: CNSN (the code used on the plot is CN), USAF/USGS (GT), GSN-IRIS/IDA (II), GSN-IRIS/USGS (IU), USNSN (US) and LODORE (XT). The stations are located at epicentral distances ranging between 95° and 127°, where the core-reflected waves ScS, $sScS$ and core-diffracted waves S_{diff}, sS_{diff} can easily be identified. In Fig. 14 we compare data to synthetic seismograms computed in the 3D hybrid model. We also display the 1D synthetic seismograms obtained in PREM as a reference. For most of the stations, it is clear that the 3D model performs better than PREM in explaining both time delays and amplitudes. This is particularly true for stations LMN and BOSA at large epicentral distance, where the effect on the amplitude is the largest. Note that slow regions are systematically associated with amplitudes higher than in PREM (e.g., YKW3, LMN) and fast regions with smaller amplitudes than in PREM (e.g., BOSA). Notice however that only first-order characteristics are reproduced by the 3D synthetic seismograms. More detailed analysis reveals that time shifts are sometimes too large (e.g., WMQ) or that both amplitude and phase are poorly fit (e.g., BW06 and TLY). The second phase, sS_{diff}, is generally poorly modeled. One of the reasons for this discrepancy is that sS_{diff} spends significant time in the strongly heterogeneous upper mantle, which is not accounted for in our 3D hybrid model.

7 CONCLUSIONS AND PERSPECTIVES

We have given an overview of the application of the spectral-element method (SEM) to realistic problems in regional and global seismology. We have shown examples of spectral-element calculations and have illustrated the ability of the method to provide a reference solution in 3D heterogeneous models of the Earth. The method has been extended for example to include the dynamics of the rupture in seismic source studies (Ampuero 2002; Vilotte & Festa 2004). With the increasing computational power available, SEM-based inversions have started to appear, with the first SEM-based moment tensor inversions in a 3D model (Liu et al. 2004) as well as SEM adjoint formulations for seismic tomography (Tromp et al. 2005) and SEM tomographic methods based on source stacking (Capdeville et al. 2005).

The source code, called SPECFEM3D, of our implementation of the SEM for parallel computers is freely available for academic, non-commercial research from `www.geodynamics.org`.

ACKNOWLEDGMENTS

The authors would like to thank Barbara Romanowicz and Yuancheng Gung for providing the NACT and PAVA synthetic seismograms of Figure 12, Akiko Toh for providing Figure 13, and Christine Bernardi and Yvon Maday for fruitful discussions. Comments by two anonymous reviewers and by editor Valérie Maupin as well as careful reading by Alexandre Fournier improved the manuscript. The material presented in section 6.1 is part of a working program supported by the European InterReg SISMOVALP project.

REFERENCES

Aki, K. & Richards, P. G., 1980, *Quantitative seismology, theory and methods*, W. H. Freeman, San Francisco.

Alford, R., Kelly, K., & Boore, D., 1974, Accuracy of finite difference modeling of the acoustic wave equation, *Geophysics*, **39**, 834–842.

Alterman, Z. & Karal, F. C., 1968, Propagation of elastic waves in layered media by finite difference methods, *Bull. Seismol. Soc. Am.*, **58**, 367–398.

Ampuero, J.-P., 2002, *Étude physique et numérique de la nucléation des séismes (A physical and numerical study of earthquake nucleation)*, Ph.D. thesis, Institut de Physique du Globe, Paris, France.

Bao, H., Bielak, J., Ghattas, O., Kallivokas, L. F., O'Hallaron, D. R., Shewchuk, J. R., & Xu, J., 1998, Large-scale simulation of elastic wave propagation in heterogeneous media on parallel computers, *Comput. Methods Appl. Mech. Engrg.*, **152**, 85–102.

Bard, P.-Y. & Bouchon, M., 1980, The seismic response of sediment-filled valleys, Part 1: The case of incident SH waves, *Bull. Seismol. Soc. Am.*, **70**, 1263–1286.

Bard, P.-Y. & Bouchon, M., 1980, The seismic response of sediment-filled valleys, Part 2: The case of incident P and SV waves, *Bull. Seismol. Soc. Am.*, **70**, 1921–1941.

Bassin, C., Laske, G., & Masters, G., 2000, The current limits of resolution for surface wave tomography in North America, *EOS*, **81**, F897.

Basu, U. & Chopra, A. K., 2003, Perfectly matched layers for time-harmonic elastodynamics of unbounded domains: theory and finite-element implementation, *Comput. Methods Appl. Mech. Engrg.*, **192**, 1337–1375.

Basu, U. & Chopra, A. K., 2004, Perfectly matched layers for transient elastodynamics of unbounded domains, *Int. J. Numer. Meth. Engng.*, **59**, 1039–1074.

Bécache, E., Fauqueux, S., & Joly, P., 2003, Stability of Perfectly Matched Layers, group velocities and anisotropic waves, *J. Comput. Phys.*, **188**(2), 399–433.

Bérenger, J. P., 1994, A Perfectly Matched Layer for the absorption of electromagnetic waves, *J. Comput. Phys.*, **114**, 185–200.

Bérenger, J. P., 1996, Three-dimensional Perfectly Matched Layer for the absorption of electromagnetic waves, *J. Comput. Phys.*, **127**, 363–379.

Bermúdez, A. & Rodríguez, R., 1994, Finite element computation of the vibration modes of a fluid-solid system, *Comput. Methods Appl. Mech. Engrg.*, **119**, 355–370.

Bittencourt, M. L., 2005, Fully tensorial nodal and modal shape functions for triangles and tetrahedra, *Int. J. Numer. Meth. Engng.*, **63**(11), 1530–1558.

Bouchon, M., 1996, The discrete wave number formulation of boundary integral equations and boundary element methods: a review with applications to the simulation of seismic wave propagation in complex geological structures, *Pure Appl. Geophys.*, **148**(1), 3–20.

Bouchon, M. & Sánchez-Sesma, F. J., 2006, Boundary-integral equations and boundary-element methods in elastodynamics, in *Advances in Wave Propagation in Heterogeneous Media*, Advances in Geophysics, Elsevier.

Canuto, C., Hussaini, M. Y., Quarteroni, A., & Zang, T. A., 1988, *Spectral methods in fluid dynamics*, Springer-Verlag, New York.

Capdeville, Y., Chaljub, E., Vilotte, J. P., & Montagner, J. P., 2003, Coupling the spectral element method with a modal solution for elastic wave propagation in global Earth models, *Geophys. J. Int.*, **152**, 34–67.

Capdeville, Y., To, A., & Romanowicz, B., 2003, Coupling spectral elements and modes in a spherical Earth: an extension to the 'sandwich' case, *Geophys. J. Int.*, **154**, 44–57.

Capdeville, Y., Gung, Y., & Romanowicz, B., 2005, Towards global Earth tomography using the spectral element method: a technique based on source stacking, *Geophys. J. Int.*, **162**, 541–554.

Carcione, J. M., 1994, The wave equation in generalized coordinates, *Geophysics*, **59**, 1911–1919.

Carcione, J. M., Kosloff, D., & Kosloff, R., 1988, Wave propagation simulation in an elastic anisotropic (transversely isotropic) solid, *Q. J. Mech. Appl. Math.*, **41**(3), 319–345.

Chaljub, E., 2000, *Modélisation numérique de la propagation d'ondes sismiques en géométrie sphérique : application à la sismologie globale (Numerical modeling of the propagation of seismic waves in spherical geometry: application to global seismology)*, Ph.D. thesis, Université Paris VII Denis Diderot, Paris, France, in French.

Chaljub, E. & Tarantola, A., 1997, Sensitivity of SS precursors to topography on the upper-mantle 660-km discontinuity, *Geophys. Res. Lett.*, **24**(21), 2613–2616.

Chaljub, E. & Valette, B., 2004, Spectral element modelling of three-dimensional wave propagation in a self-gravitating Earth with an arbitrarily stratified outer core, *Geophys. J. Int.*, **158**, 131–141.

Chaljub, E., Capdeville, Y., & Vilotte, J. P., 2003, Solving elastodynamics in a fluid-solid heterogeneous sphere: a parallel spectral element approximation on non-conforming grids, *J. Comput. Phys.*, **187**(2), 457–491.

Chaljub, E., Cornou, C., Guéguen, P., Causse, M., & Komatitsch, D., 2005, Spectral-element modeling of 3D wave propagation in the alpine valley of Grenoble, France, in *Geophysical Research Abstracts*, vol. 7, 05225, EGU 2nd general assembly, Wien, Austria.

Chen, X., 2006, Generation and propagation of seismic SH waves in multilayered media with irregular interfaces, in *Advances in Wave Propagation in Heterogeneous Media*, Advances in Geophysics, Elsevier.

Clévédé, E., Mégnin, C., Romanowicz, B., & Lognonné, P., 2000, Seismic waveform modeling and surface wave tomography in a three-dimensional Earth: asymptotic and non-asymptotic approaches, *Phys. Earth Planet. Inter.*, **119(1)**, 37–56.

Cohen, G. & Fauqueux, S., 2000, Mixed finite elements with mass lumping for the transient wave equation, *J. Comput. Acoust.*, **8**(1), 171–188.

Cohen, G. & Fauqueux, S., 2005, Mixed spectral finite elements for the linear elasticity system in unbounded domains, *SIAM Journal on Scientific Computing*, **26**(3), 864–884.

Cohen, G., Joly, P., & Tordjman, N., 1993, Construction and analysis of higher-order finite elements with mass lumping for the wave equation, in *Proceedings of the second international conference on mathematical and numerical aspects of wave propagation*, edited by R. Kleinman, pp. 152–160, SIAM, Philadephia, PA.

Cohen, G., Joly, P., Roberts, J. E., & Tordjman, N., 2001, Higher-order triangular finite elements with mass lumping for the wave equation, *SIAM Journal on Numerical Analysis*, **38**(6), 2047–2078.

Collino, F. & Monk, P., 1998, Optimizing the Perfectly Matched Layer, *Comput. Methods Appl. Mech. Engrg.*, **164**, 157–171.

Collino, F. & Tsogka, C., 2001, Application of the PML absorbing layer model to the linear elastodynamic problem in anisotropic heterogeneous media, *Geophysics*, **66**(1), 294–307.

Cornou, C., Bard, P.-Y., & Dietrich, M., 2003, Contribution of dense array analysis to the identification and quantification of basin-edge-induced waves, Part II: Application to the Grenoble basin (French Alps), *Bull. Seismol. Soc. Am.*, **93**(6), 2624–2648.

Courant, R., Friedrichs, K. O., & Lewy, H., 1928, Über die partiellen Differenzengleichungen der mathematischen Physik, *Mathematische Annalen*, **100**, 32–74, in German.

Cowling, T. G., 1941, The non-radial oscillations of polytropic stars, *Mon. Not. Roy. Astron. Soc.*, **101**, 369–373.

Dahlen, F. A. & Tromp, J., 1998, *Theoretical Global Seismology*, Princeton University Press, Princeton.

Day, S. M., 1998, Efficient simulation of constant Q using coarse-grained memory variables, *Bull. Seismol. Soc. Am.*, **88**, 1051–1062.

Day, S. M. & Bradley, C., 2001, Memory-efficient simulation of anelastic wave propagation, *Bull. Seismol. Soc. Am.*, **91**, 520–531.

Deville, M. O., Fischer, P. F., & Mund, E. H., 2002, *High-Order Methods for Incompressible Fluid Flow*, Cambridge University Press, Cambridge, United Kingdom.

Dhatt, G. & Touzot, G., 1984, *The finite element method displayed*, John Wiley and sons, New York.

Dziewonski, A. M. & Anderson, D. L., 1981, Preliminary reference Earth model, *Phys. Earth Planet. Inter.*, **25**, 297–356.

Emmerich, H. & Korn, M., 1987, Incorporation of attenuation into time-domain computations of seismic wave fields, *Geophysics*, **52**, 1252–1264.

Faccioli, E., Maggio, F., Paolucci, R., & Quarteroni, A., 1997, 2D and 3D elastic wave propagation by a pseudo-spectral domain decomposition method, *J. Seismol.*, **1**, 237–251.

Favier, N., Chevrot, S., & Komatitsch, D., 2004, Near-field influences on shear wave splitting and traveltime sensitivity kernels, *Geophys. J. Int.*, **156**, 467–482.

Festa, G. & Nielsen, S., 2003, PML absorbing boundaries, *Bull. Seismol. Soc. Am.*, **93**, 891–903.

Festa, G. & Vilotte, J. P., 2005, The Newmark scheme as velocity-stress time-staggering: an efficient PML implementation for spectral element simulations of elastodynamics, *Geophys. J. Int.*, **161**, 789812.

Frankel, A., 1993, Three-dimensional simulations of ground motions in the San Bernardino valley, California, for hypothetical earthquakes on the San Andreas fault, *Bull. Seismol. Soc. Am.*, **83**, 1020–1041.

Frankel, A. & Vidale, J., 1992, A three-dimensional simulation of seismic waves in the Santa Clara valley, California, from the Loma Prieta aftershock, *Bull. Seismol. Soc. Am.*, **82**, 2045–2074.

Funaro, D., 1992, *Polynomial approximation of differential equations*, vol. 8 of **Lecture notes in physics**, Springer Verlag, Heidelberg.

Furumura, M., Kennett, B. L. N., & Furumura, T., 1999, Seismic wavefield calculation for laterally heterogeneous Earth models–II. the influence of upper mantle heterogeneity, *Geophys. J. Int.*, **139**(3), 623–644.

Furumura, T., Kennett, B. L. N., & Furumura, M., 1998, Seismic wavefield calculation for laterally heterogeneous whole Earth models using the pseudospectral method, *Geophys. J. Int.*, **135**(3), 845–860.

Giraldoa, F. & Warburton, T., 2005, A nodal triangle-based spectral element method for the shallow water equations on the sphere, *J. Comput. Phys.*, **207**(1), 129–150.

Givoli, D., 1992, *Numerical Methods for Problems in Infinite Domains*, Elsevier Science Publishers, Amsterdam, The Netherlands.

Graves, R. W. & Day, S. M., 2003, Stability and accuracy of coarse-grain viscoelastic simulations, *Bull. Seismol. Soc. Am.*, **93**, 283–300.

Gropp, W., Lusk, E., & Skjellum, A., 1994, *Using MPI, portable parallel programming with the Message-Passing Interface*, MIT Press, Cambridge, USA.

Hamdi, M. A., Ousset, Y., & Verchery, G., 1978, A displacement method for the analysis of vibrations of coupled fluid-structure systems, *Int. J. Numer. Meth. Engng.*, **13**, 139–150.

Hughes, T. J. R., 1987, *The finite element method, linear static and dynamic finite element analysis*, Prentice-Hall International, Englewood Cliffs, New Jersey, USA.

Igel, H. & Weber, M., 1995, SH-wave propagation in the whole mantle using high-order finite differences, *Geophys. Res. Lett.*, **22**, 731–734.

Igel, H. & Weber, M., 1996, P-SV wave propagation in the whole mantle using high-order finite differences: application to lowermost mantle structure, *Geophys. Res. Lett.*, **23**, 415–418.

Jobert, N., Gaulon, R., Dieulin, A., & Roult, G., 1977, Sur les ondes de très longue période, caractéristiques du manteau supérieur, *Comptes rendus Acad. Sci. Paris*, **Série B, 285**, 49–51, in French.

Kane, C., Marsden, J., Ortiz, M., & West, M., 2003, Variational integrators and the Newmark algorithm for conservative and dissipative mechanical systems, *Int. J. Numer. Meth. Engng.*, **49**(10), 1295–1325.

Karypis, G. & Kumar, V., 1998, A fast and high-quality multilevel scheme for partitioning irregular graphs, *SIAM Journal on Scientific Computing*, **20**(1), 359–392.

Karypis, G. & Kumar, V., 1998, Multilevel k-way partitioning scheme for irregular graphs, *Journal of Parallel and Distributed Computing*, **48**(1), 96–129.

Kelly, K. R., Ward, R. W., Treitel, S., & Alford, R. M., 1976, Synthetic seismograms: a finite difference approach, *Geophysics*, **41**, 2–27.

Knupp, P. M., 1999, Applications of mesh smoothing: copy, morph, and sweep on unstructured quadrilateral meshes, *Int. J. Numer. Meth. Engng.*, **45**(1), 37–45.

Komatitsch, D., 1997, *Méthodes spectrales et éléments spectraux pour l'équation de l'élastodynamique 2D et 3D en milieu hétérogène (Spectral and spectral-element methods for the 2D and 3D elastodynamics equations in heterogeneous media)*, Ph.D. thesis, Institut de Physique du Globe, Paris, France, in French, 187 pages.

Komatitsch, D. & Tromp, J., 1999, Introduction to the spectral-element method for 3-D seismic wave propagation, *Geophys. J. Int.*, **139**, 806–822.

Komatitsch, D. & Tromp, J., 2002, Spectral-element simulations of global seismic wave propagation-I. Validation, *Geophys. J. Int.*, **149**, 390–412.

Komatitsch, D. & Tromp, J., 2002, Spectral-element simulations of global seismic wave propagation-II. 3-D models, oceans, rotation, and self-gravitation, *Geophys. J. Int.*, **150**, 303–318.

Komatitsch, D. & Tromp, J., 2003, A Perfectly Matched Layer absorbing boundary condition for the second-order seismic wave equation, *Geophys. J. Int.*, **154**, 146–153.

Komatitsch, D. & Vilotte, J. P., 1998, The spectral-element method: an efficient tool to simulate the seismic response of 2D and 3D geological structures, *Bull. Seismol. Soc. Am.*, **88**(2), 368–392.

Komatitsch, D., Barnes, C., & Tromp, J., 2000, Wave propagation near a fluid-solid interface: a spectral element approach, *Geophysics*, **65**(2), 623–631.

Komatitsch, D., Martin, R., Tromp, J., Taylor, M. A., & Wingate, B. A., 2001, Wave propagation in 2-D elastic media using a spectral element method with triangles and quadrangles, *J. Comput. Acoust.*, **9**(2), 703–718.

Komatitsch, D., Ritsema, J., & Tromp, J., 2002, The spectral-element method, Beowulf computing, and global seismology, *Science*, **298**, 1737–1742.

Komatitsch, D., Tsuboi, S., Ji, C., & Tromp, J., 2003, A 14.6 billion degrees of freedom, 5 teraflops, 2.5 terabyte earthquake simulation on the Earth Simulator, *Proceedings of the ACM/IEEE Supercomputing SC'2003 conference*, published on CD-ROM and at www.sc-conference.org/sc2003.

Komatitsch, D., Liu, Q., Tromp, J., Süss, P., Stidham, C., & Shaw, J. H., 2004, Simulations of ground motion in the Los Angeles basin based upon the spectral-element method, *Bull. Seismol. Soc. Am.*, **94**, 187–206.

Kumazawa, M. & Anderson, O. L., 1969, Elastic moduli, pressure derivates and temperature derivates of single-crystal olivine and single-crystal forstite, *J. Geophys. Res.*, **74**, 5961–5972.

Li, X. D. & Romanowicz, B., 1995, Comparison of global waveform inversions with and without considering cross–branch modal coupling, *Geophys. J. Int.*, **121**, 695–709.

Li, X. D. & Tanimoto, T., 1993, Waveforms of long-period body waves in a slightly aspherical Earth model, *Geophys. J. Int.*, **112**, 92–102.

Liu, H. P., Anderson, D. L., & Kanamori, H., 1976, Velocity dispersion due to anelasticity: implications for seismology and mantle composition, *Geophys. J. R. Astron. Soc.*, **47**, 41–58.

Liu, Q., Polet, J., Komatitsch, D., & Tromp, J., 2004, Spectral-element moment-tensor inversions for earthquakes in Southern California, *Bull. Seismol. Soc. Am.*, **94**, 1748–1761.

Lysmer, J. & Drake, L. A., 1972, A finite element method for seismology, in *Methods in Computational Physics*, vol. 11, Academic Press, New York, USA.

Madariaga, R., 1976, Dynamics of an expanding circular fault, *Bull. Seismol. Soc. Am.*, **65**, 163–182.

Maday, Y. & Patera, A. T., 1989, Spectral element methods for the incompressible Navier-Stokes equations, in *State of the art survey in computational mechanics*, pp. 71–143, A. K. Noor and J. T. Oden editors.

Maday, Y. & Rønquist, E. M., 1990, Optimal error analysis of spectral methods with emphasis on non-constant coefficients and deformed geometries, *Comput. Methods Appl. Mech. Engrg.*, **80**, 91–115.

Marfurt, K. J., 1984, Accuracy of finite-difference and finite-element modeling of the scalar wave equation, *Geophysics*, **49**, 533–549.

Mégnin, C. & Romanowicz, B., 2000, The 3D shear velocity structure of the mantle from the inversion of body, surface and higher modes wave forms, *Geophys. J. Int.*, **143**, 709–728.

Mercerat, E. D., Vilotte, J. P., & Sánchez-Sesma, F. J., 2005, Triangular spectral-element simulation of 2D elastic wave propagation using unstructured triangular grids, *Geophys. J. Int.*, submitted.

Newmark, N. M., 1959, A method of computation for structural dynamics, in *Engineering mechanics division: Proceedings of the American Society of Civil Engineers*, pp. 67–93.

Nicoud, G., Royer, G., Corbin, J.-C., Lemeille, F., & Paillet, A., 2002, Creusement et remplissage de la vallée de l'Isère au Quaternaire récent: apports nouveaux du forage GMB1 (1999) dans la région de Grenoble (France), *Géologie de la France*, **4**, 39–49, in French.

Olsen, K. B., 2000, Site amplification in the Los Angeles basin from three-dimensional modeling of ground motion, *Bull. Seismol. Soc. Am.*, **90**, S77–S94.

Olsen, K. B. & Archuleta, R. J., 1996, 3-D simulation of earthquakes on the Los Angeles fault system, *Bull. Seismol. Soc. Am.*, **86**(3), 575–596.

Pasquetti, R. & Rapetti, F., 2004, Spectral element methods on triangles and quadrilaterals: comparisons and applications, *J. Comput. Phys.*, **198**(1), 349–362, doi: 10.1016/j.jcp.2004.01.010.

Patera, A. T., 1984, A spectral element method for fluid dynamics: laminar flow in a channel expansion, *J. Comput. Phys.*, **54**, 468–488.

Phinney, R. A. & Burridge, R., 1973, Representation of elastic-gravitational excitation of a spherical Earth model by generalized spherical harmonics, *Geophys. J. R. Astron. Soc.*, **34**, 451–487.

Pitarka, A., Irikura, K., Iwata, T., & Sekiguchi, H., 1998, Three-dimensional simulation of the near-fault ground motion for the 1995 Hyogo-ken Nanbu (Kobe), Japan, earthquake, *Bull. Seismol. Soc. Am.*, **88**, 428–440.

Priolo, E., Carcione, J. M., & Seriani, G., 1994, Numerical simulation of interface waves by high-order spectral modeling techniques, *J. Acoust. Soc. Am.*, **95**(2), 681–693.

Ritsema, J., Van Heijst, H. J., & Woodhouse, J. H., 1999, Complex shear velocity structure imaged beneath Africa and Iceland, *Science*, **286**, 1925–1928.

Ronchi, C., Ianoco, R., & Paolucci, P. S., 1996, The "Cubed Sphere": a new method for the solution of partial differential equations in spherical geometry, *J. Comput. Phys.*, **124**, 93–114.

Rosat, S., Hinderer, J., & Rivera, L., 2003, First observation of ${}_2S_1$ and study of the splitting of the football mode ${}_0S_2$ after the June 2001 Peru earthquake of magnitude 8.4, *Geophys. Res. Lett.*, **30**(21), 2111, doi:10.1029/2003GL018304.

Sadourny, R., 1972, Conservative finite-difference approximations of the primitive equations on quasi-uniform spherical grids, *Monthly Weather Review*, **100**, 136–144.

Seriani, G., 1998, 3-D large-scale wave propagation modeling by a spectral element method on a Cray T3E multiprocessor, *Comput. Methods Appl. Mech. Engrg.*, **164**, 235–247.

Seriani, G. & Priolo, E., 1994, A spectral element method for acoustic wave simulation in heterogeneous media, *Finite Elements* *in Analysis and Design*, **16**, 337–348.

Tautges, T. J., 2004, MOAB-SD: integrated structured and unstructured mesh representation, *Engineering with Computers*, **20**(3), 286–293, doi: 10.1007/s00366-004-0296-0.

Taylor, M., Tribbia, J., & Iskandarani, M., 1997, The spectral element method for the shallow water equation on the sphere, *J. Comput. Phys.*, **130**, 92–108.

Taylor, M. A., Wingate, B. A., & Vincent, R. E., 2000, An algorithm for computing Fekete points in the triangle, *SIAM Journal on Numerical Analysis*, **38**(5), 1707–1720.

Teixeira, F. L. & Chew, W. C., 1999, On causality and dynamic stability of Perfectly Matched Layers for FDTD simulations, *IEEE transactions on Microwave Theory and Techniques*, **47**(6), 775–785.

Tessmer, E. & Kosloff, D., 1994, 3-D elastic modeling with surface topography by a Chebyshev spectral method, *Geophysics*, **59**(3), 464–473.

Thouvenot, F., Fréchet, J., Jenatton, L., & Gamond, J.-F., 2003, The Belledonne border fault: identification of an active seismic strike-slip fault in the western Alps, *Geophys. J. Int.*, **155**(1), 174–192.

Tordjman, N., 1995, *Éléments finis d'ordre élevé avec condensation de masse pour l'équation des ondes (High-order finite elements with mass lumping for the wave equation)*, Ph.D. thesis, Université Paris IX Dauphine, Paris, France, in French.

Toshinawa, T. & Ohmachi, T., 1992, Love-wave propagation in a three-dimensional sedimentary basin, *Bull. Seismol. Soc. Am.*, **82**(4), 1661–1677.

Tromp, J., Tape, C., & Liu, Q., 2005, Seismic tomography, adjoint methods, time reversal and banana-doughnut kernels, *Geophys. J. Int.*, **160**(1), 195–216, doi: 10.1111/j.1365-246X.2004.02453.x.

Tsuboi, S., Komatitsch, D., Ji, C., & Tromp, J., 2003, Spectral-element simulations of the November 3, 2002, Denali, Alaska earthquake on the Earth Simulator, *Phys. Earth Planet. Inter.*, **139**, 305–313.

Valette, B., 1986, About the influence of prestress upon the adiabatic perturbations of the Earth, *Geophys. J. R. Astron. Soc.*, **85**, 179–208.

Valette, B., 1989, Spectre des vibrations propres d'un corps élastique, auto-gravitant, en rotation uniforme et contenant une partie fluide (Free oscillations spectrum of an elastic, self-gravitating, uniformly rotating body with a fluid inclusion), *C. R. Acad. Sci. Paris*, **309**, 419–422, in French.

Vallon, M., 1999, Estimation de l'épaisseur d'alluvions et sédiments quaternaires dans la région grenobloise par inversion des anomalies gravimétriques (Estimation of the thickness of alluvial and quaternary deposits in the Grenoble area by inverting gravimetric anomalies), Tech. rep., LGGE, IPSN/CNRS, Université Joseph Fourier, in French.

Vilotte, J.-P. & Festa, G., 2004, Spectral element simulation of rupture dynamics on curvilinear faults, *EOS*, **85**(47), Abstract S32B–08.

Virieux, J., 1986, *P-SV* wave propagation in heterogeneous media: velocity-stress finite-difference method, *Geophysics*, **51**, 889–901.

Winton, S. C. & Rappaport, C. M., 2000, Specifying PML conductivities by considering numerical reflection dependencies, *IEEE transactions on Antennas and Propagation*, **48**(7), 1055–1063.

Woodhouse, J. H. & Dziewonski, A. M., 1984, Mapping the upper mantle: Three-dimensional modeling of Earth structure by inversion of seismic waveforms, *J. Geophys. Res.*, **89**, 5953–5986.

Zeng, X., 1996, *Finite difference modeling of viscoelastic wave propagation in a generally heterogeneous medium in the time domain, and a dissection method in the frequency domain*, Ph.D. thesis, University of Toronto, Canada.

Zingg, D. W., 2000, Comparison of high-accuracy finite-difference methods for linear wave propagation, *SIAM Journal on Scientific Computing*, **22**(2), 476–502, doi: 10.1137/S1064827599350320.

Zingg, D. W., Lomax, H., & Jurgens, H., 1996, High-accuracy finite-difference schemes for linear wave propagation, *SIAM Journal on Scientific Computing*, **17**(2), 328–346, doi: 10.1137/S1064827594267173.

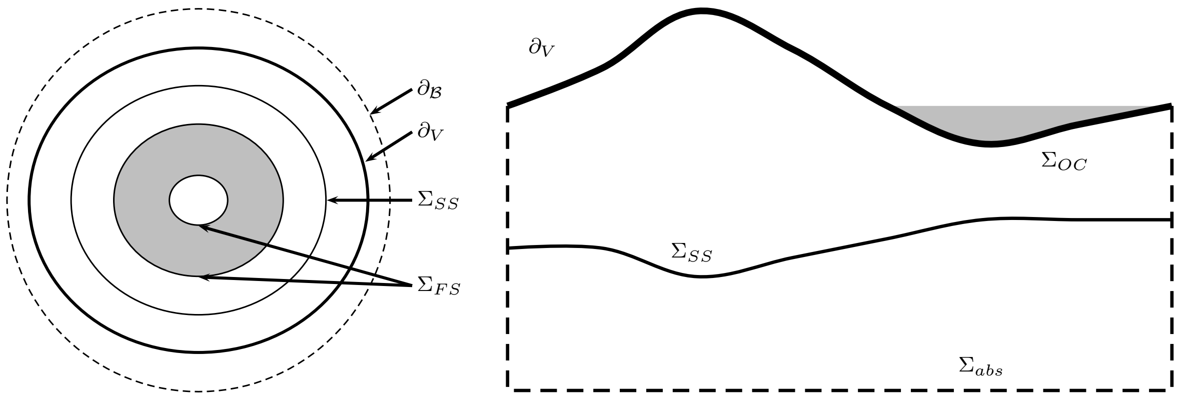

Figure 1. Sketch of a typical problem geometry for global (left) and regional (right) simulations of wave propagation. Shaded areas denote fluid regions, i.e., the outer core and the oceans. Dashed lines are specific to each problem: the spherical outer boundary $\partial_{\mathcal{B}}$ is relevant for the treatment of self-gravitation at the global scale, while the absorbing boundary Σ_{abs} only matters for regional applications.

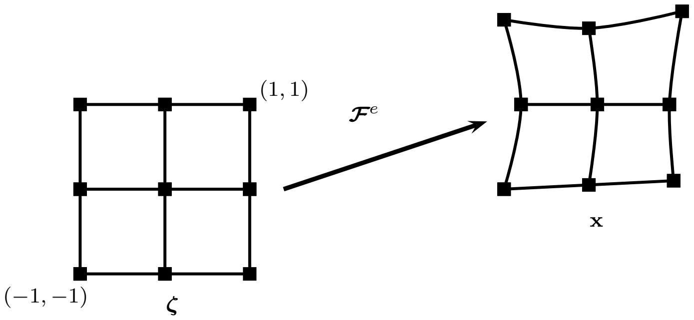

Figure 2. Example of a 2D mapping on the reference square based upon 9 control or 'anchor' points.

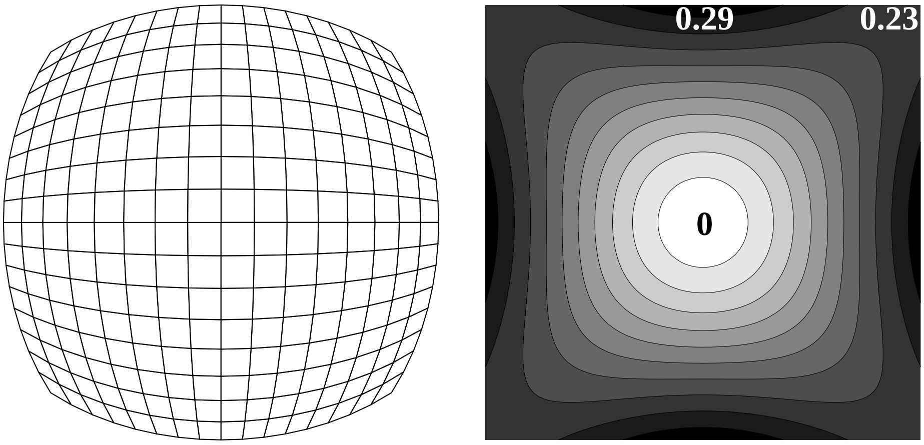

Figure 3. Left: One-sixth of the surface of a sphere is tiled with a 16×16 quadrangular grid obtained by applying the 'cubed sphere' transformation. Right: Contour lines of area variation within the grid show that the area of each element is at most 29% smaller than a reference element that would be located at the center of the face.

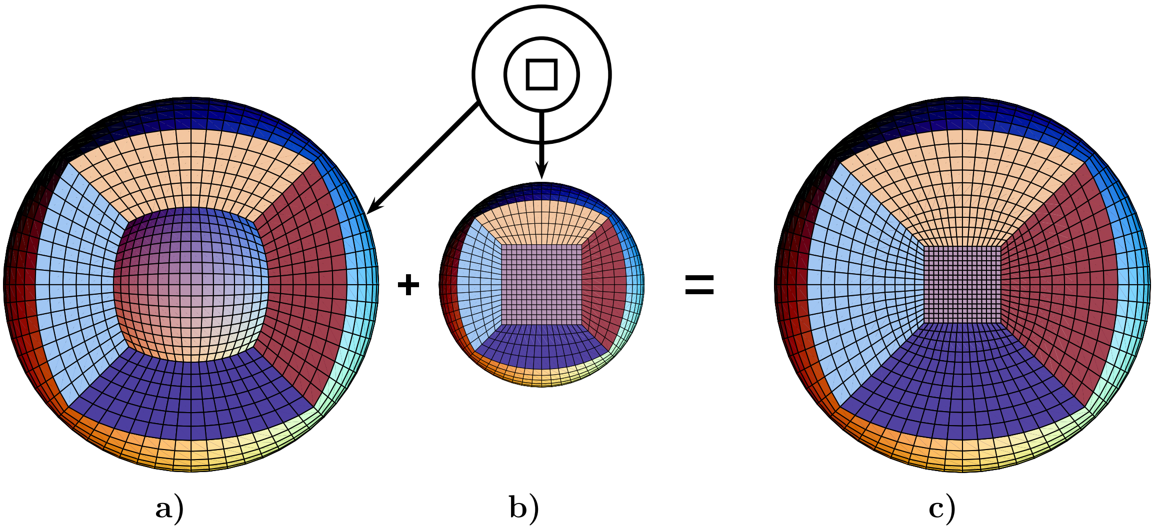

Figure 4. Process used to build a mesh of hexahedra for a sphere: a) the spherical interfaces are tiled based upon the cubed sphere transformation, and then connected in the radial direction; b) a cube is inserted in the center; c) the final 3D mesh of the sphere is obtained by connecting a) and b).

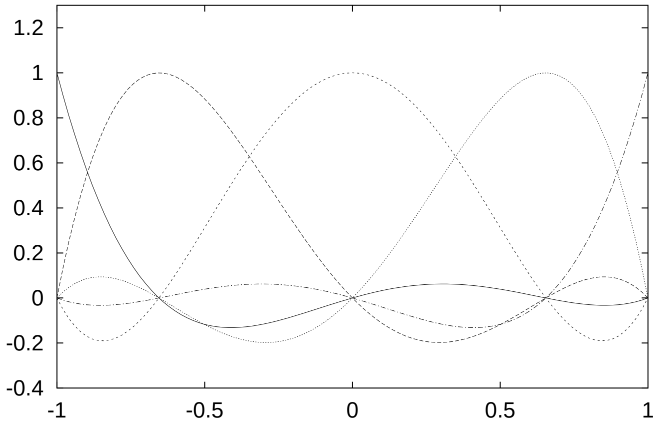

Figure 5. Lagrange interpolants of degree $N = 4$ on the reference interval $\Lambda = [-1, 1]$. The corresponding $N + 1 = 5$ Gauss-Lobatto-Legendre points can be seen along the horizontal axis. All Lagrange polynomials are, by definition, equal to 1 or 0 at each of these points. Note that the first and last points are exactly -1 and 1.

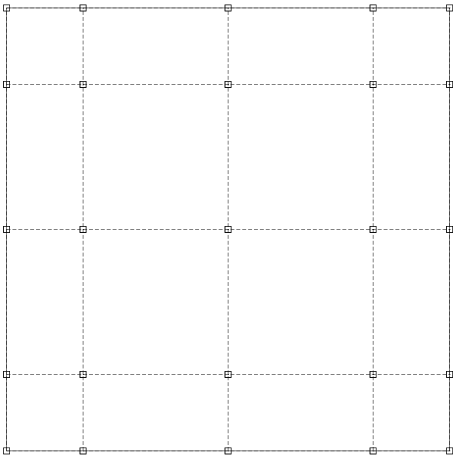

Figure 6. When a polynomial degree N is used to discretize the wave field, each 3D spectral element contains a grid of $(N+1)^3$ Gauss-Lobatto-Legendre points, and each 2D face of an element contains a grid of $(N+1)^2$ Gauss-Lobatto-Legendre points, as illustrated here in the case of $N=4$. By construction, these points are non-evenly spaced.

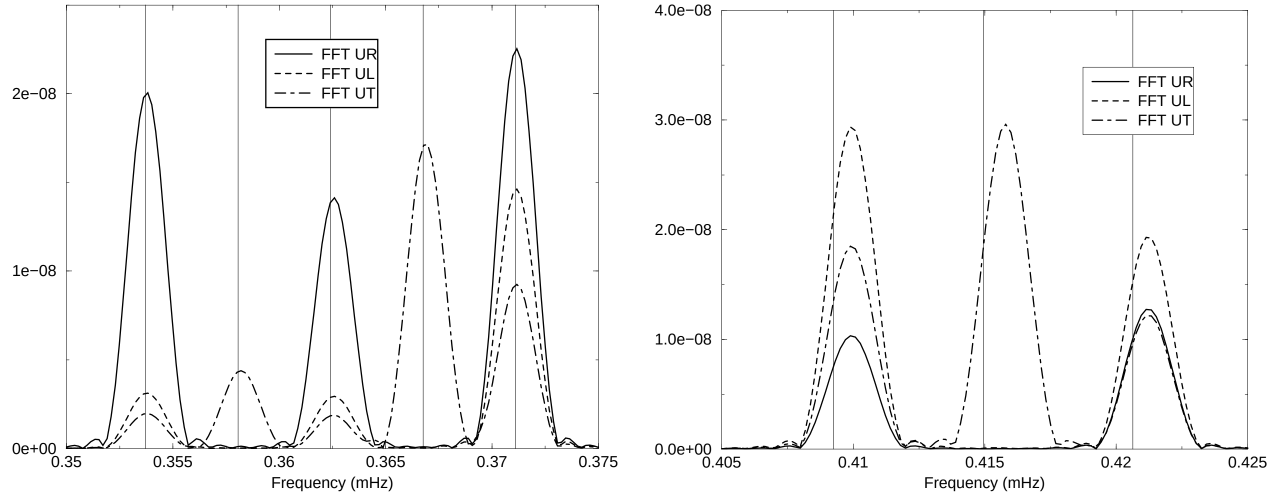

Figure 7. Amplitude spectrum of spectral-element synthetic seismograms computed at a station located 90° away from the source. The left and right frequency windows display the ${}_0S_2$ and ${}_2S_1$ modes, respectively. The different singlets appear on the radial (solid line), longitudinal (dashed line) and transverse (dot-dashed line) components for this geometry. The vertical lines show the first-order theoretical prediction of the Coriolis splitting. The difference with the synthetic values illustrates the magnitude of higher-order effects. Note that the eigenvalues given here are slightly higher than real values because self-gravitation has not been accounted for in our calculations.

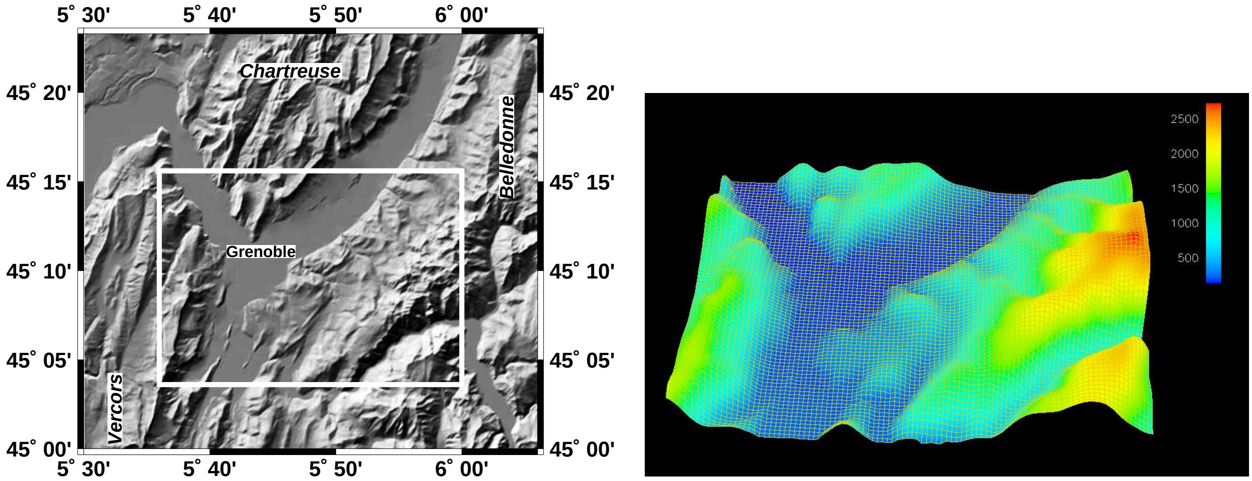

Figure 8. Left: Topographic map of the Alps showing the city of Grenoble surrounded by the Vercors, Chartreuse and Belledonne massifs. The white square denotes the edges of the computing grid used to simulate ground motion. Right: Surface view of the spectral-element mesh used to compute synthetic waveforms accurate up to approximately 1 Hz. The mesh contains 96×80 surface elements. The vertical exaggeration factor is 5 and a spatial Gaussian filter has been applied to smooth sharp topographic variations.

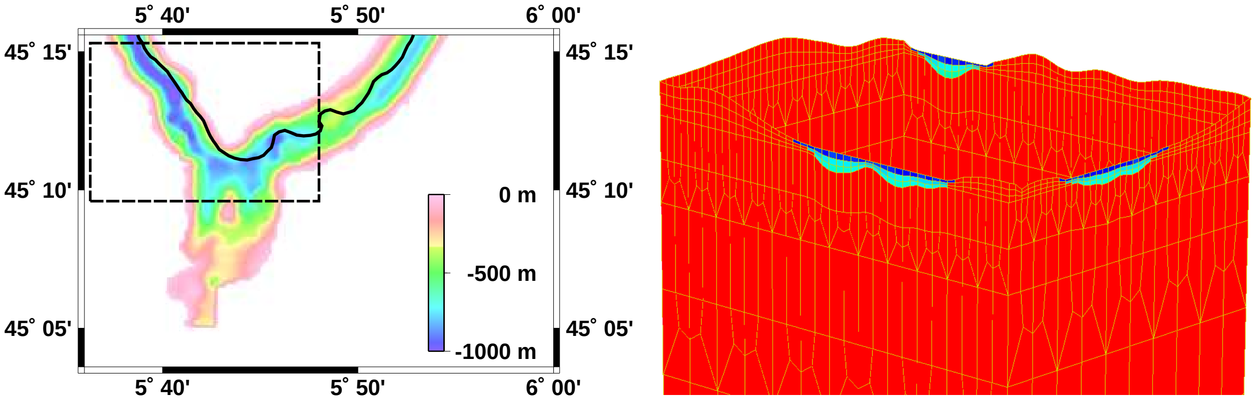

Figure 9. Left: Map of the shape of the bedrock obtained by inverting gravimetric measurements over the Grenoble valley. The maximum sediment thickness, which is located in the western part of the 'Y' shaped valley, exceeds 1000 m. The black line represents the Isère river. Right: view from the south-east with no vertical exaggeration of a cross section through the spectral-element mesh (in the area indicated by the dashed lines in the left picture). Red indicates elements that intersect the bedrock, whereas blue represents elements located entirely within the sediments. The mesh is coarsened twice in depth to adapt it to the variations of seismic wavelengths within the model. The sediment/bedrock interface is honored exactly (i.e., the elastic parameters are discontinuous across the interface in the mesh) for depths greater than 220 m. At shallower depths (in particular near valley edges) the contrast between bedrock and sediments is smeared out due to the use of high-order ($N = 4$) polynomial interpolation within each spectral element.

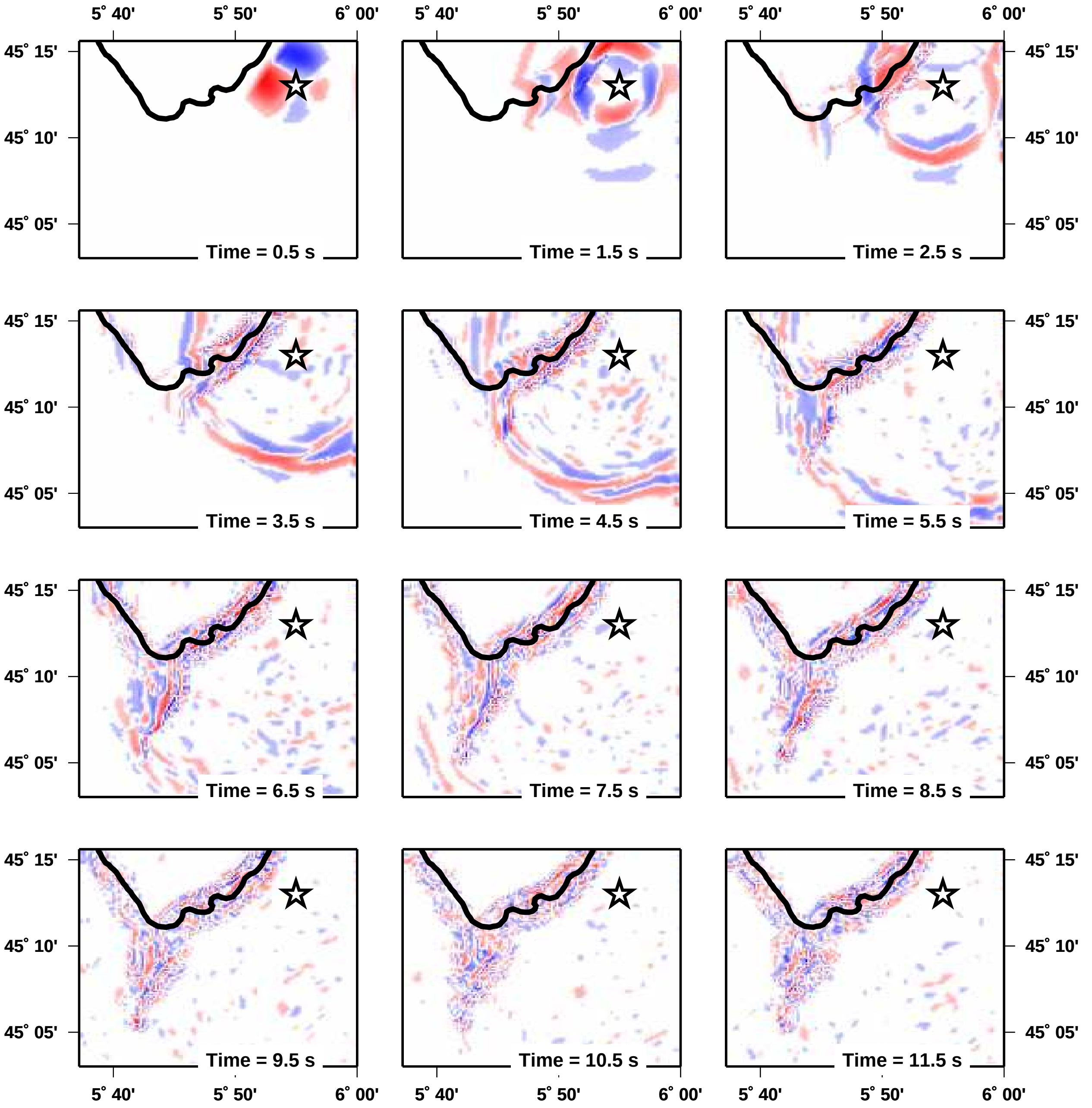

Figure 10. Time evolution of the vertical component of synthetic ground velocity simulated for the April 26, 2003, $M_L = 2.9$, Lancey event, whose epicenter is indicated by the black and white star. Red and blue colors denote upward and downward motion, respectively. The radiation pattern of this strike-slip event is clearly seen at time 0.5 s. At times between 1.5 s and 3.5 s, the P and S wavefronts are deflected by the slow wave speeds in the basin. Energy diffracted off the edges of the basin and traveling as surface waves can be observed before 8.5 s. Note the complex shape of the wave field, with almost no coherent pattern after 10 s of propagation.

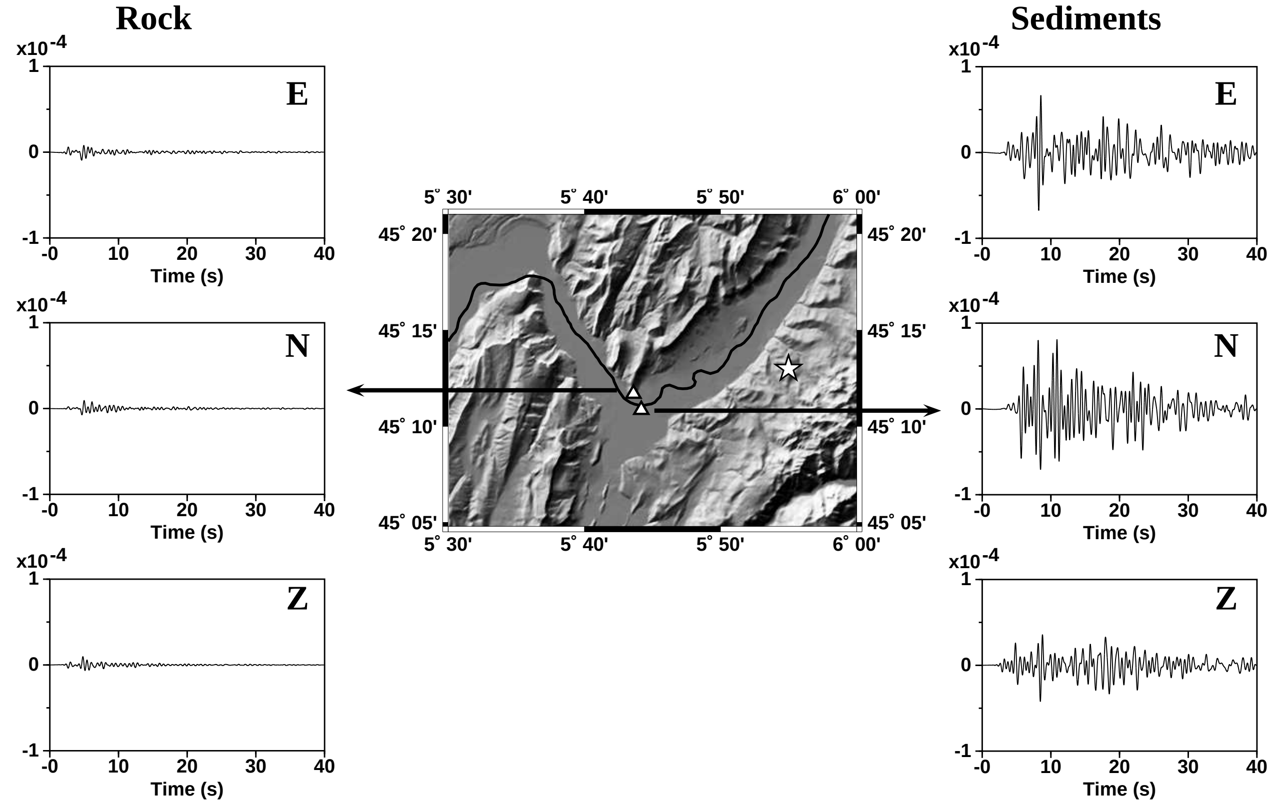

Figure 11. Time series of ground velocity (in m.s^{-1}) computed for the April 26, 2003, $M_L = 2.9$ Lancey event, whose epicenter is indicated by the black and white star, at two stations of the French accelerometric network (black and white triangles). The left records correspond to a rock site, and the right records to a site located in the center of the basin, where the sediment thickness exceeds 800 m. Both synthetic seismograms have been bandpass-filtered between 0.1 Hz and 2 Hz using a six-pole two-pass Butterworth filter. Note the strong amplification as well as the increased duration of the signal recorded in the basin even though the two sites are only separated by a distance of about 1 km.

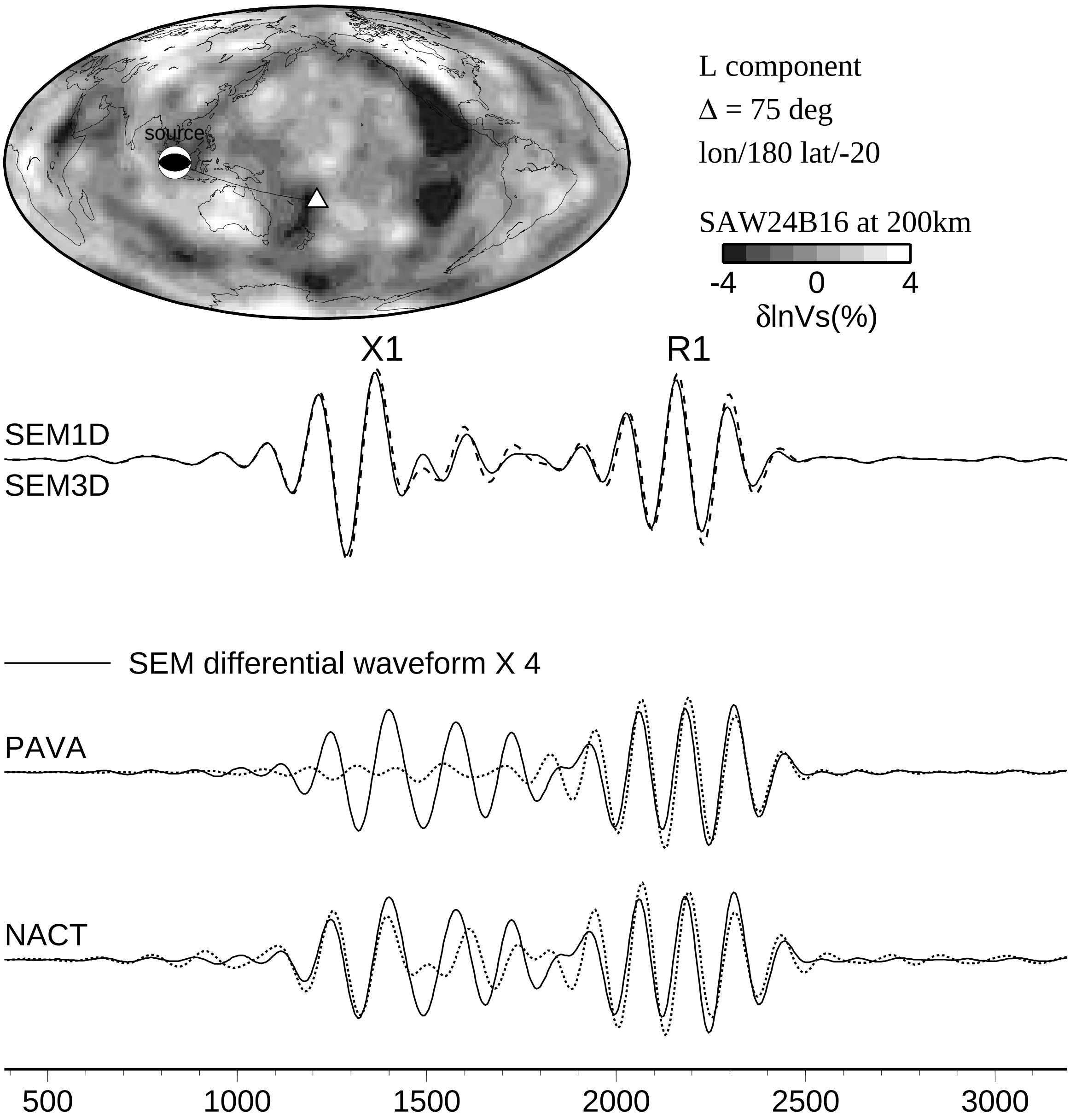

Figure 12. Comparison of the two asymptotic methods PAVA and NACT on a 3D synthetic example in tomographic model SAW24B16. The map shows the path selected. In this long-period test (100 s and above) only the longitudinal component is displayed. The top panel shows the SEM synthetic seismograms computed in the reference model (solid line) and in the 3D model (dotted line). The last two panels show differential seismograms (3D results minus 1D results) obtained based upon the PAVA (middle) and NACT (bottom) methods and amplified by a factor of four. In each case, the solid line represents the differential synthetic seismograms obtained based upon the SEM. As expected, NACT performs better than PAVA in fitting the high-order harmonics (here the X wave). In this example, the spectral-element solution is used as a 3D reference to estimate the fit obtained.

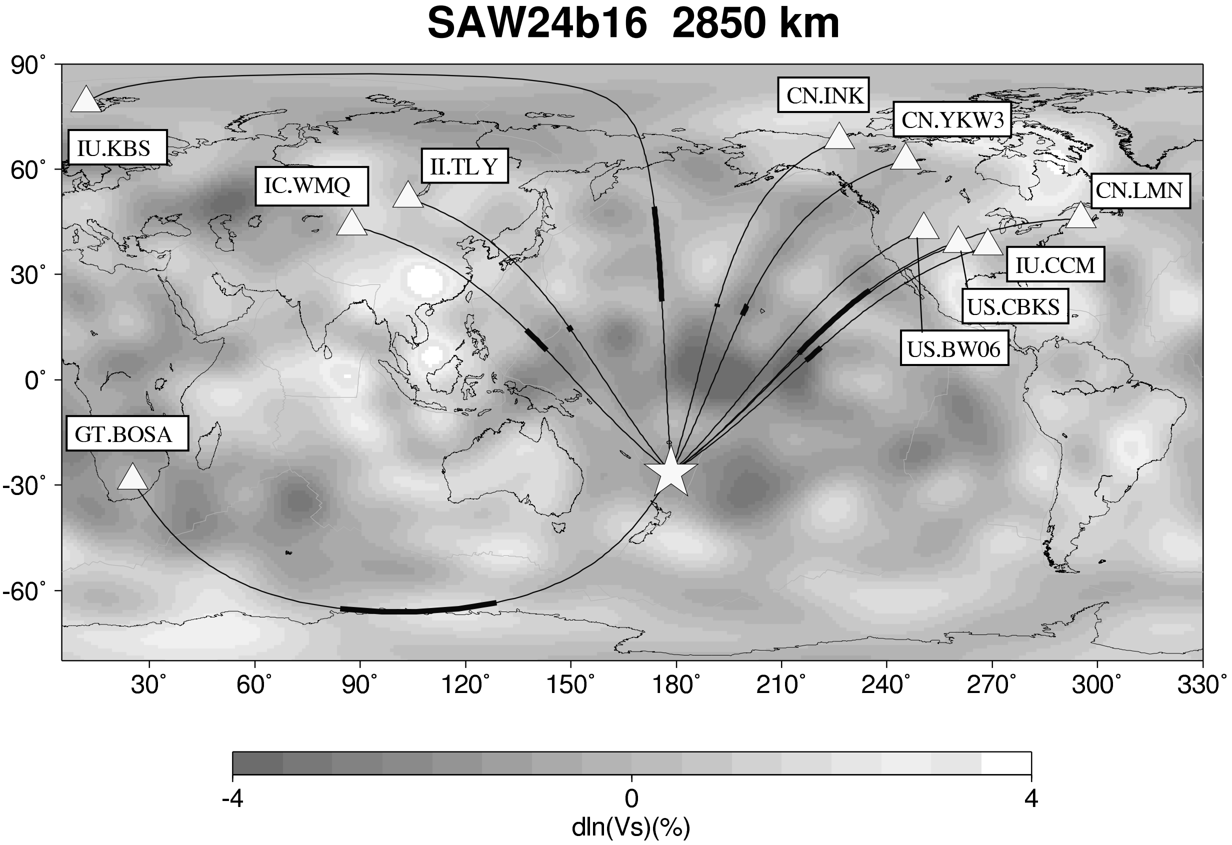

Figure 13. Configuration of source and stations used to model wave propagation in the D″ layer. The background model is tomographic model SAW24B16 above the CMB. The paths between the source and the stations are plotted, and the part of the path that samples the D″ layer in PREM is represented in bold.

Figure 14. Comparison between data (thin solid line), synthetic seismograms computed in PREM (dotted line) and synthetic seismograms computed in a velocity model that is heterogeneous in the 370 km above the CMB (bold solid line) for the transverse component of displacement. In the D$''$ layer, perturbations relative to PREM are taken from tomographic model SAW24B16. The traces are aligned with respect to the $S_{\rm diff}$ arrival time and represented with increasing azimuth. On each trace, the first energy arrival is a combination of the core reflected S wave (ScS) and the S wave diffracted at the CMB ($S_{\rm diff}$). The second energy arrival corresponds to a similar interference between phases ($sScS$ and $sS_{\rm diff}$) that have first been reflected off the Earth's surface. Except in a few places (e.g., at station TLY), the 3D model generally improves the fit to data for the first energy arrival, both in amplitude and phase. The prediction of the 3D model is not as good for the second energy arrival, because the effect of the crust and mantle (which is not accounted for in our calculation) represents an important contribution to the misfit between synthetic seismograms and data.

APPENDIX A: MODIFIED HOOKE'S LAW

A1 Intrinsic attenuation

In an anelastic medium, the stress tensor is defined from the entire strain history. We can write this dependence as

$$\sigma(t) \;=\; \left([M\,H] \star \dot{\varepsilon}\right)(t) \;=\; \left(\left[M\,\delta + \dot{M}\,H\right] \star \varepsilon\right)(t) \;, \tag{A.1}$$

where σ stands for either hydrostatic or deviatoric stress, ε for the corresponding strain and M for the bulk or shear modulus. The star $\star$ denotes time convolution, δ is the Dirac delta distribution and H is the Heaviside distribution that ensures the causality of the stress-strain relation.

Following Liu et al. (1976), we simulate a constant Q attenuation mechanism by choosing a stress relaxation function $M(t)$ in (A.1) that is the superimposition of L standard linear solids. This can be formally written as

$$M(t) \;=\; M_R \;+\; \sum_{\ell=1}^{L} a_\ell\; e^{-t/\tau_\ell} \;, \tag{A.2}$$

or

$$M(t) \;=\; M_U \;-\; \sum_{\ell=1}^{L} a_\ell\; \left(1 - e^{-t/\tau_\ell}\right) \;, \tag{A.3}$$

where M_R (resp. M_U) stands for the relaxed (resp. unrelaxed) elastic modulus and τ_ℓ denotes the relaxation time of the l-th mechanism. The a_ℓ are coefficients that can be chosen in order to fit a given Q law. Their sum is the modulus defect: $\sum_{\ell=1}^{L} a_\ell \;=\; \delta M \;=\; M_U - M_R$. A constant Q law is well approximated if the inverse relaxation times (i.e., the central frequencies of the L mechanisms) are chosen to be evenly distributed in logarithmic scale (e.g., Emmerich & Korn 1987).

Next, we set $\Phi(t) = \dot{M}\,H\,(t) = \sum_{\ell=1}^{L} \Phi_\ell\,H\,(t)$ where

$$\Phi_\ell(t) \;=\; -\frac{a_\ell}{\tau_\ell}\, e^{-t/\tau_\ell} \;, \tag{A.4}$$

and we define a set of L memory variables (e.g., Carcione et al. 1988) by

$$R_l(t) \;=\; \left([\Phi_l\,H] \star \varepsilon\right)\;(t) \;. \tag{A.5}$$

The stress-strain relation (A.1) then becomes

$$\sigma(t) \;=\; M_U\,\varepsilon\,(t) + \sum_{\ell=1}^{L} R_\ell\,(t) \;, \tag{A.6}$$

The advantage of the modified stress-strain relation (A.6) is that it can be implemented in the time domain because each memory variable R_ℓ obeys the first-order differential equation:

$$\dot{R}_\ell(t) + \frac{1}{\tau_\ell} R_\ell(t) \;=\; -\frac{a_\ell}{\tau_\ell}\,\varepsilon(t) \;. \tag{A.7}$$

In practice, three or four mechanisms are used to obtain a quality factor that is almost constant in the frequency range of interest (e.g., Emmerich & Korn 1987; Komatitsch & Tromp 2002a). In terms of implementation, the implication is that the memory variables need to be stored on the grid, and therefore the memory requirements increase substantially compared to purely elastic simulations. It is worth mentioning that to alleviate this burden, memory variables can be spread across an element, such that one carries only one memory variable at each grid point, obtaining the expected anelastic behavior in average (Zeng 1996; Day 1998; Day & Bradley 2001; Graves & Day 2003). In our implementation however, we do not spread the memory variables across the grid.

A2 Fictitious attenuation in absorbing layers

In regional applications, non-reflecting conditions must be defined at the boundaries of the computational domain to mimic an unbounded medium. Among the different methods that can be used, we focus here on the Perfectly Matched Layer (PML) method, originally developed by Bérenger (1994, 1996) in the context of electromagnetics, because it is the most efficient.

The PML can be viewed as an analytical continuation of the real coordinates in the complex space, where the stretching s is given by (e.g., Teixeira & Chew 1999):

$$\tilde{x}_j = \int_0^{x_j} 1 + i\,\frac{s_j\,(\xi)}{\omega} d\xi \;. \tag{A.8}$$

Here ξ stands for the distance away from the interface between the PML and the regular domain in the j direction, and ω denotes angular frequency. With this definition, the amplitude of a plane wave defined by $\exp\left(i(\omega t - \mathbf{k}\cdot\mathbf{x})\right)$ decreases along the j direction by the frequency-independent factor $\exp\left(-\frac{k_j}{\omega}\int s_j(\xi)d\xi\right)$.

The mapping (A.8) induces a metric change $\tilde{\mathbf{G}} = \mathbf{\Lambda}\,\mathbf{G}\,\mathbf{\Lambda}$, where $\mathbf{G}$ is the Euclidean metric and

$$\mathbf{\Lambda} = \begin{pmatrix} s_1 & 0 & 0 \\ 0 & s_2 & 0 \\ 0 & 0 & s_3 \end{pmatrix} . \tag{A.9}$$

The conservation of momentum gives (see e.g., Festa & Vilotte 2005):

$$i\,\omega\,\rho\,\det(\mathbf{\Lambda})\,\dot{\mathbf{u}} \;=\; \nabla\cdot\left(\tilde{\mathbf{T}}(\mathbf{u})\right) \tag{A.10}$$

where $\tilde{\mathbf{T}} = \det(\mathbf{\Lambda})\,\mathbf{\Lambda}^{-1}\mathbf{T}$ is the Piola transform of $\mathbf{T}$. The elastic properties of the medium are given by the symmetric second Piola tensor $\mathbf{T}' = \tilde{\mathbf{T}}\,\mathbf{\Lambda}^{-1}$, which satisfies Hooke's law:

$$\mathbf{T}' \;=\; \tilde{\mathbf{c}} : \nabla\mathbf{u} \tag{A.11}$$

where the fourth-order elastic tensor $\mathbf{c}$ is defined by

$$\tilde{c}_{ijkl} = \det(\mathbf{\Lambda})\,c_{mnsl}\;\mathbf{\Lambda}^{-1}_{mi}\,\mathbf{\Lambda}^{-1}_{nj}\,\mathbf{\Lambda}^{-1}_{sk} \;. \tag{A.12}$$

When going back to the time domain, the convolution can be avoided by splitting kinematic and dynamic fields into non-physical components following the directions of the derivatives normal and parallel to the interface between the PML and the regular domain. The original equations can then be written as (e.g., Festa & Nielsen 2003):

$$\rho(\ddot{\mathbf{u}}_i^{(m)} + d_m\,\dot{\mathbf{u}}_i^{(m)}) = \;\frac{\partial \mathbf{T}_{ij}}{\partial x_j}\,\delta_{jm} \;, \tag{A.13}$$

$$\dot{\mathbf{T}}_{ij}^{(m)} + d_m\,\mathbf{T}_{ij}^{(m)} \;=\; c_{ijkl}\,\frac{\partial \dot{\mathbf{u}}_l}{\partial x_k}\,\delta_{km} \;, \tag{A.14}$$

where the superscripts refer to the only derivative that is kept on the right-hand side. The total fields are finally obtained by summing the split components:

$$\dot{\mathbf{u}}_i = \sum_{m=1}^{3}\dot{\mathbf{u}}_i^{(m)} \;, \quad \mathbf{T}_{ij} = \sum_{m=1}^{3}\mathbf{T}_{ij}^{(m)} \;. \tag{A.15}$$

It is worth noting that unsplit PML formulations are currently under development for the seismic wave equation. Such formulations would have the advantage of reducing the memory cost of the technique because one would not need to define additional arrays to store the split components of the fields. They would also be simpler to implement in existing codes without PML because these are based on the total field.

APPENDIX B: DTN OPERATORS

B1 Dynamic coupling

Consider the coupling of a spectral-element solution with a normal-mode solution in global seismology. Such coupling is said to be dynamic because it depends on time (an example of static coupling is given in the next section). Such a coupling strategy is useful when some regions of the Earth can be assumed to be spherically symmetric. In those regions, the solution can therefore be sought in the frequency domain and expanded onto the basis of generalized spherical harmonics $\mathbf{Y}_{\ell m}$ (e.g., Phinney & Burridge 1973), where ℓ and m stand for the angular and azimuthal degree, respectively. We thus face the problem of coupling a solution in the space-time domain with a solution in the spectral-frequency domain. Several options are available for that purpose. To derive the traction boundary condition on Γ, one can either convert the incoming displacement $\mathbf{u}^V$ in the spectral-frequency domain, apply the DtN operator to obtain the traction in the spectral-frequency domain, and then convert it back to the space-time domain. The DtN operator can also be converted to the space-time domain and applied to the incoming displacement $\mathbf{u}^V$, which implies a series of convolution in time and space. Even if not strictly equivalent numerically, both solutions require an infinite sum over the spherical harmonic degree ℓ and an unbounded integration over frequency, which both need to be truncated in order to be performed numerically. In the remainder of this section, we will assume that the DtN operator is applied in the space-time domain.

We start with the expression of the operator in the spectral-frequency domain. Denoting $\mathbf{u}_\omega(\mathbf{x}) = \mathbf{u}(\mathbf{x},\omega)$, the counterpart of Eq. (40) in the frequency domain can be written as

$$\boldsymbol{\mathcal{D}}^W_\omega(\mathbf{u}^W_\omega) \;=\; \mathbf{T}(\mathbf{u}^W_\omega)\cdot\hat{\mathbf{n}} \;, \tag{B.1}$$

which we expand on the basis of generalized spherical harmonics as

$$\boldsymbol{\mathcal{D}}^W_\omega(\mathbf{u}^W_\omega) \;=\; \sum_{\ell=0}^{\infty}\sum_{m=-\ell}^{+\ell}{}_\ell\boldsymbol{\mathcal{D}}^W_\omega(\mathbf{u}^W_\omega) : \mathbf{Y}_{\ell m} \;, \tag{B.2}$$

where the colon denotes the dot product with the canonical basis (see e.g., Dahlen & Tromp 1998, p. 901 for details).

Note that the operator is local in the spectral-frequency domain, in the sense that the ℓm coefficients of traction at a given frequency ω only depend on the same coefficients of displacement at the same frequency. Note also that ${}_\ell\boldsymbol{\mathcal{D}}_\omega^W$ has no dependence on the azimuthal degree m because of the spherical symmetry of W.

The DtN in the space-time domain is obtained by an inverse Fourier transform:

$$\boldsymbol{\mathcal{D}}_t^W(\mathbf{u}^V_{t'\leq t}) \;=\; \sum_{\ell=0}^{\infty}\sum_{m=-\ell}^{+\ell}\int_{-\infty}^{+\infty} {}_\ell\boldsymbol{\mathcal{D}}_\omega^W(\mathbf{u}_\omega^W) : \mathbf{Y}_{\ell m}\, e^{i\omega t} d\omega \;. \tag{B.3}$$

In order to be performed numerically, the sum over ℓ needs to be truncated to a cutoff angular degree ℓ_{max} large enough to provide an accurate approximation of the DtN operator in the space domain. In a spherically-symmetric model and far enough from the source, the relation between the corner frequency of the source and the maximum angular degree of the wave field is known from the dispersion relation. In practice, when dealing with a 3D Earth model, we apply this 1D criterion to the spherical average of the 3D model in V.

Computing the inverse Fourier transform (B.3) requires one to circumvent two issues. First, because W is bounded, ${}_\ell\boldsymbol{\mathcal{D}}_\omega^W$ is undefined for the set of frequencies corresponding to the eigenmodes of W with a homogeneous Dirichlet boundary condition on Γ. To perform the frequency integration, the DtN operator is split into a discrete spectrum for which the Cauchy theorem is used, and a continuous spectrum for which a fast Fourier transform is applied. Second, the infinite frequency range in Eq. (B.3) cannot be truncated without affecting the causality of the DtN operator. Let ω_c stand for a frequency greater than the corner frequency of the source, then the truncated DtN operator obtained by replacing the infinite frequency interval in (B.3) by $[-\omega_c, \omega_c]$ is not causal. To solve this problem, Capdeville et al. (2003a) introduced a regularized, causal operator based upon an asymptotic approximation at high frequency. This regularized operator ${}_r\boldsymbol{\mathcal{D}}_t$ is defined by

$${}_r\boldsymbol{\mathcal{D}}_\omega^W \;=\; \boldsymbol{\mathcal{D}}_\omega^W - {}_a\boldsymbol{\mathcal{D}}_\omega^W \;, \tag{B.4}$$

where ${}_a\boldsymbol{\mathcal{D}}_w^W$ stands for an asymptotic approximation of the operator based on an expansion in powers of $i\omega$. By definition, the regularized operator converges toward zero at high frequency. The final operator $\boldsymbol{\mathcal{D}}_t^W$ is obtained by summing the inverse Fourier transforms:

$$\boldsymbol{\mathcal{D}}_t^W \;=\; {}_r\boldsymbol{\mathcal{D}}_t^W + {}_a\boldsymbol{\mathcal{D}}_t^W \;. \tag{B.5}$$

The reader is referred to Capdeville et al. (2003a) for details about the regularization procedure applied to the DtN operator, and to Capdeville et al. (2003b) for the extension to the case where the source is located within W.

B2 Static coupling

Another example of DtN coupling arises when accounting for the perturbation of the gravitational potential in the wave equation, or when computing the gravity field induced by a 3D distribution of density. Both problems involve a scalar potential that is defined everywhere in space, whereas the computational domain is bounded. A coupling strategy with the analytical solution of the exterior problem allows one to circumvent this issue.

Let W denote the region exterior to $\mathcal{B}$: $W = \mathbb{R}^3 \setminus \mathcal{B}$, so that the coupling interface $\Gamma = \partial_{\mathcal{B}}$ is the sphere of radius b (see Fig. 1). The coupling strategy is to solve Poisson's equation in $\mathcal{B}$ with a condition on Γ involving the normal derivative of the potential (i.e., the Neumann variable for this problem) and to solve Laplace's equation in W with a prescribed potential (the Dirichlet variable) on the boundary.

The DtN operator for the Poisson-Laplace equation is thus $\mathcal{D}^W(\chi^W) = \nabla\chi^W \cdot \hat{\mathbf{n}}$, where χ stands for either the mass redistribution potential $\psi(\mathbf{u})$ or the non-rotating gravity potential ϕ'. Because the coupling interface is spherical, the expression of the DtN operator is readily obtained in the spherical harmonics basis (see Chaljub & Valette 2004):

$$\mathcal{D}^W(\chi^W) \;=\; -\frac{1}{b}\sum_{\ell=0}^{\infty}(\ell+1)\sum_{m=-\ell}^{\ell}\chi_{lm}^W(b)\,\mathcal{Y}_{\ell m}(\theta,\varphi) \;, \tag{B.6}$$

where $\mathcal{Y}_{\ell m}$ denotes the real spherical harmonic of degree ℓ and order m, (θ, φ) are the spherical coordinates and $\chi_{\ell m}^W(b) = \int_\Gamma \chi^W \mathcal{Y}_{\ell m}\, dS$.

Finally, the boundary condition to be used to solve for the non-rotating gravity potential in $\mathcal{B}$ is

$$\nabla\phi'^{\mathcal{B}} \cdot \hat{\mathbf{n}} \;=\; \mathcal{D}^W(\phi'^{\mathcal{B}}) \;, \tag{B.7}$$

and that for the mass redistribution potential is

$$\nabla\psi(\mathbf{u})^{\mathcal{B}} \cdot \hat{\mathbf{n}} \;=\; \mathcal{D}^W(\psi(\mathbf{u})^{\mathcal{B}}) \;+\; 4\pi G\rho^{\mathcal{B}}\,\mathbf{u}^{\mathcal{B}} \cdot \hat{\mathbf{n}} \;, \tag{B.8}$$

according to the jump condition (37) and assuming that the exterior domain W is a vacuum, i.e., $\rho^W = 0$. Note that the second term on the right-hand side of Eq. (B.8) only matters when topography or ellipticity is considered at the surface of the Earth.

B3 Ocean load approximation

More than 71% of the surface of the Earth is covered by oceans. At short period, one may want to take into account the effect of these oceans on global seismic wave propagation (e.g., their effect on the reflection coefficient of phases reflected at the ocean bottom, such as PP, SS and SP, as well as on the dispersion of Rayleigh waves).

Following Komatitsch & Tromp (2002b), we assume that the oceans are incompressible, i.e., that the entire water column moves as a whole as a result of the normal displacement $\mathbf{u} \cdot \hat{\mathbf{n}}$ of the sea floor. This approximation, which is accurate for seismic wavelengths larger than the thickness of the oceans, is valid down to periods of approximately 20 s, but not below. With such an assumption, we can only reproduce the effect of the load at the ocean floor, but we cannot model phases such as the tsunami that propagate in the oceans themselves.

Assuming a homogeneous fluid layer (therefore neutrally stratified, i.e., its Brunt-Väisälä frequency N is zero in Eq. (17)) and neglecting the redistribution of mass, the wave equation (5) in the oceans reduces to

$$\ddot{\mathbf{u}} + 2\boldsymbol{\Omega} \times \dot{\mathbf{u}} = -\boldsymbol{\nabla}\left(\frac{\delta p}{\rho} - \mathbf{u} \cdot \mathbf{g}\right) , \qquad \text{(B.9)}$$

where δp is the Lagrangian perturbation of pressure defined by (14).

Let h_w denote the local thickness of the oceans (i.e., of the equivalent local water column), which can be taken from a bathymetry map. If one considers the normal component of Eq. (B.9), integrates over the column of water and takes into account the variations of gravity with radius, one can show that locally

$$\delta p \;=\; \rho_w \, h_w \, \ddot{\mathbf{u}} \cdot \hat{\mathbf{n}} + 2\rho_w \, h_w \, (\boldsymbol{\Omega} \times \dot{\mathbf{u}}) \cdot \hat{\mathbf{n}} + 4\pi G \rho_w^2 \, h_w \, \mathbf{u} \cdot \hat{\mathbf{n}}, \qquad \text{(B.10)}$$

where ρ_w denotes the density of sea water ($\rho_w \simeq 1020$ kg.m^{-3}). In practice, at periods above typically 20 s the ocean load is a small effect, and the gravity and rotation terms in (B.10) are even smaller corrections that can be safely ignored. We therefore get the following equation at the ocean floor

$$\mathbf{T}(\mathbf{u}) \cdot \hat{\mathbf{n}} \;=\; -\, \delta p \, \hat{\mathbf{n}} \;\simeq\; -\, \rho_w \, h_w \, (\ddot{\mathbf{u}} \cdot \hat{\mathbf{n}}) \, \hat{\mathbf{n}} \; . \qquad \text{(B.11)}$$